ORIGINAL ARTICLE

Check for updates

Ground-motion prediction models for induced earthquakes in the Groningen gas field, the Netherlands

Julian J. Bommer [iD] · Peter J. Stafford [iD] ·
Adrian Rodriguez-Marek [iD] · Michail Ntinalexis [iD] · Pauline P. Kruiver [iD] ·
Benjamin Edwards [iD] · Bernard Dost [iD] · Jan van Elk

Abstract Small-magnitude earthquakes induced by gas production in the Groningen field in the Netherlands have prompted the development of seismic risk models that serve both to estimate the impact of these events and to explore the efficacy of different risk mitigation strategies. A core element of the risk modelling is ground-motion prediction models (GMPM) derived from an extensive database of recordings obtained from a dense network of accelerographs installed in the field. For the verification of damage claims, an empirical GMPM for peak ground velocity (PGV) has been developed, which predicts horizontal PGV as a function of local magnitude, M_L; hypocentral distance, R_{hyp}; and the time-averaged shear-wave velocity over the upper 30 m, V_{S30}. For modelling the risk due to potential induced and triggered earthquakes of larger magnitude, a GMPM for response spectral accelerations has been developed from regressions on the outputs from finite-rupture simulations of motions at a deeply buried rock horizon. The GMPM for rock motions is coupled with a zonation map defining frequency-dependent non-linear amplification factors to obtain estimates of surface motions in the region of thick deposits of soft soils. The GMPM for spectral accelerations is formulated within a logic-tree framework to capture the epistemic uncertainty associated with extrapolation from recordings of events of $M_L \leq 3.6$ to much larger magnitudes.

Keywords Induced earthquakes · Groningen gas field · Ground-motion prediction · Site response · Seismic risk analysis

Highlights

• Recorded ground motions due to small-magnitude, shallow-focus induced earthquakes in the Groningen gas field reflect the unique upper crustal structure and thick deposits of soft soils encountered in the region and are found to be systematically different even from motions recorded in other Dutch gas fields; consequently, seismic hazard and risk analyses for Groningen require bespoke ground-motion prediction models calibrated to the specific characteristics of the field.

• An empirical model for predicting peak ground velocity as a function of magnitude, distance, and site conditions, for application to the assessment of damage claims, has been derived from a large database of recordings from induced earthquakes of local magnitude between 1.8 and 3.6; the data reveals apparent differences between recordings of different networks and alternative versions of

1 Introduction

Conventional gas production in several fields in the north and northeast of the Netherlands has resulted in induced earthquakes (van Eijs et al. 2006; van Eck et al. 2006). Natural seismicity in the Netherlands is generally confined to the south of the country (Fig. 1), a notable example being the 1992 Roermond earthquake of local magnitude M_L 5.8 and moment magnitude **M** 5.3 (Camelbeeck et al. 1994; Haak et al. 1994; Dufumier et al. 1997). The Groningen gas field, which is by far the largest in the Netherlands,

has produced the greatest number of induced earthquakes and the largest induced event in the Netherlands, namely the Huizinge earthquake of August 2012, assigned magnitudes of M_L 3.6 and **M** 3.5.

The Groningen gas reservoir is situated in the Rotliegend-Slochteren sandstone, a formation of up to ~ 300 m in thickness, located at a depth of about 3 km. The reservoir is offset in numerous locations by faults that have not been active in geologically recent times. Pressure depletion as a result of gas production has led to compaction of the reservoir that leads to

---

the empirical model additionally account for this factor.
• For risk analyses in terms of structural damage and injury, ground-motion prediction models for response spectral accelerations are required for magnitude 2.5 to above 7, to account for triggered seismicity. Finite fault simulations, calibrated to the local recordings, are used to predict motions at a buried rock horizon, and these are combined with a field zonation for frequency-dependent, non-linear amplification factors to obtain surface motions. The model is developed in a logic-tree framework to capture the uncertainty associated with the large extrapolation in magnitude.

J. J. Bommer (✉) · P. J. Stafford
Department of Civil & Environmental Engineering, Imperial College London, South Kensington Campus, London SW7 2AZ, UK
e-mail: j.bommer@imperial.ac.uk

E. Ruigrok · P. P. Kruiver · B. Dost
R&D Seismology and Acoustics, Royal Netherlands Meteorological Institute (KNMI), Utrechtseweg 297, 3731 GA De Bilt, the Netherlands
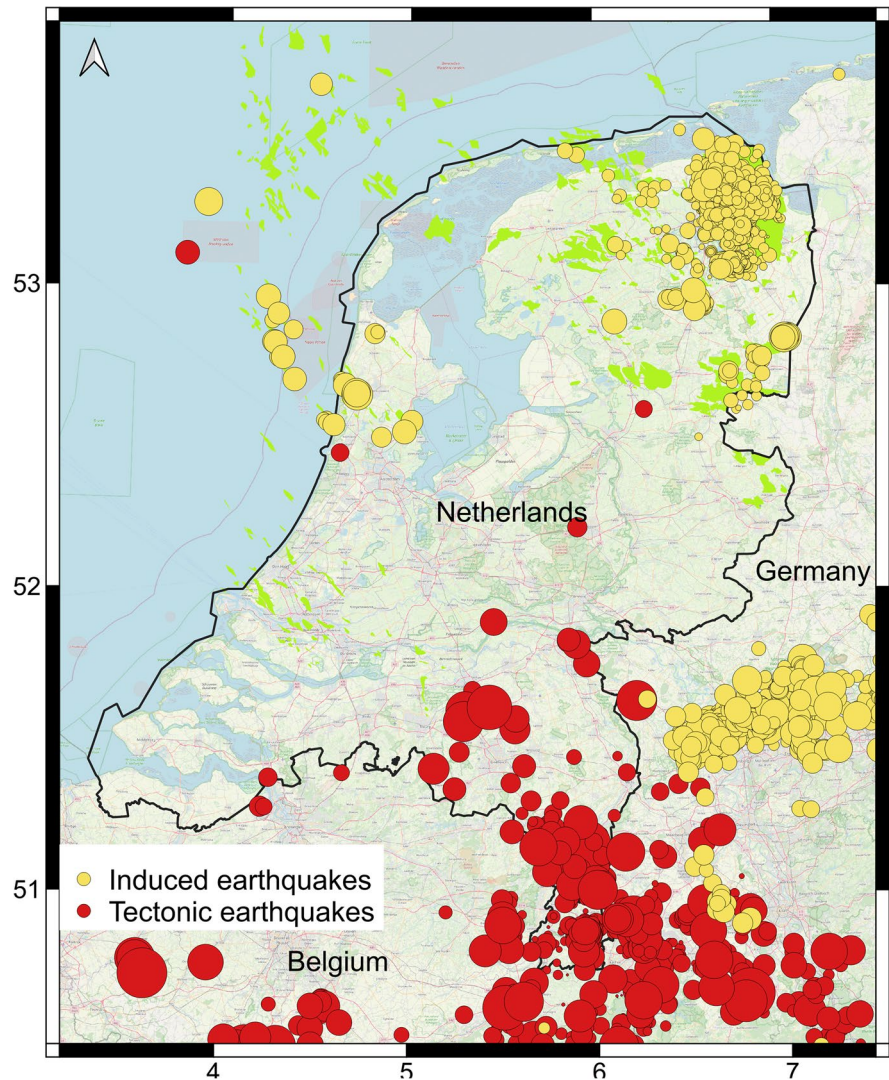
A. Rodriguez-Marek
Charles E Via, Jr., Department of Civil and Environmental Engineering, Virginia Tech, Blacksburg, VA 24061, USA

M. Ntinalexis
Independent Consultant, London, UK

B. Edwards
Department of Earth, Ocean and Ecological Sciences, University of Liverpool, Liverpool L69 3GP, UK

J. van Elk
Nederlandse Aardolie Maatschappij B.V. (NAM), Schepersmaat 2, 9405 TA Assen, the Netherlands

---

stress increases across the offsets, which has caused the reactivation of many of the faults (e.g. Buijze et al. 2017; Bourne et al. 2018). The first induced earthquake to be detected (M_L 2.4) occurred in 1991, about 28 years after production began, when the maximum reservoir compaction had reached about 20 cm (Bourne et al. 2014).

In response to the induced earthquakes, the field operator NAM (Nederlandse Aardolie Maatschappij) initiated the development of risk analysis model to estimate the impact of potential larger induced earthquakes and even larger triggered events (van Elk et al. 2017). The express purpose of the a risk model was to inform decision-making regarding risk mitigation options, through the capability to model the consequences of reduced production levels (and hence lower additional reservoir compaction) on the seismicity rates and the effects of building strengthening on reducing fragility (van Elk et al. 2019). The vital link between these two elements—the seismicity model and the exposure and fragility models—is a model for the prediction of ground-motion levels due to each earthquake scenario.

An obvious candidate for the ground-motion prediction, at least for peak ground acceleration (PGA) and velocity (PGV), were the equations derived by Dost et al. (2004) using recordings from induced earthquakes in the Roswinkel gas field supplemented by a few recordings from a swarm of tectonic earthquakes in the most southern region of the Netherlands near the city of Voerendaal (there were no ground-motion recordings in the Roermond earthquake within 50 km of the epicentre). However, the recorded motions from the Groningen field indicate systematic differences in the amplitudes of ground shaking compared to those from Roswinkel, with the Groningen motions being consistently lower, as shown in Fig. 2. The earthquakes in Roswinkel occurred at depths of about 2 km, whereas the Groningen events occur at the reservoir depth of 3 km. However, this difference in the ground motions observed from induced earthquakes in the two fields is believed to be mainly due to differences in the geology overlying the gas reservoirs. In the Groningen field, the gas-bearing sandstone, where the earthquakes originate, is situated below a thick layer of Zechstein salt (including thin layers of very high-velocity anhydrites), which has been shown to exert a pronounced influence on the propagation of seismic waves (Kraaijpoel and Dost 2013). In the Roswinkel

Fig. 1 Epicentres of natural (red) and induced (yellow) earthquakes in and around the Netherlands (KNMI). Symbol size reflects earthquake magnitude. Outlines of the gas reserves are indicated in green


gas field, however, the reservoir is situated above the high-velocity Zechstein formation. The surface soils in the Roswinkel field are generally stiffer than in Groningen, with Holocene soils (clays and peats) being largely absent; hence, greater site amplification would be expected in Groningen than in Roswinkel. These observations reinforced the decision that it was necessary to develop a Groningen-specific ground-motion prediction model (GMPM). In addition to requiring a model that captures the influence of the upper crustal structure in the Groningen field, it was also considered highly desirable to develop a GMPM to reflect the specific site response characteristics of the thick soil layers, including soft clay and peat deposits, that overlie most of the field. Consequently, ground-motion models

have been constructed that are exclusively applicable to the Groningen gas field and surrounding areas and cannot be transported to other regions. However, the framework in which the model has been developed and some of the insights obtained through this iterative process of model development may be of value to others faced with predicting ground motions from induced and triggered earthquakes.

2 An evolutionary development of ground-motion models

The GMPMs presented in this paper are the final products of an evolutionary process that commenced

Fig. 2 Comparison of recorded PGA (upper) and PGV (lower) values recorded at epicentral distances of less than 2 km from induced earthquakes in the Roswinkel and Groningen fields, plotted against magnitude. The points are plotted at values fractionally above (triangles) and below (circles) the exact magnitude in order to separate the symbols for clarity; the data shown are limited to the very short distances at which ground motions were recorded in Roswinkel
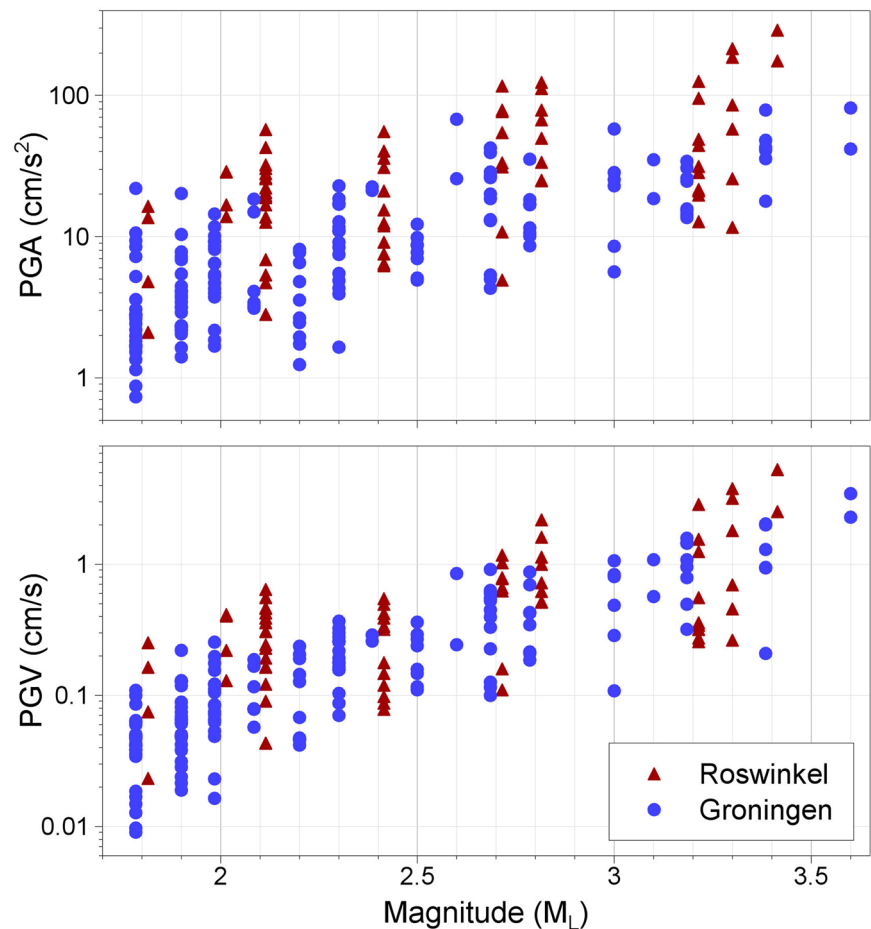
in 2013 and has passed through several iterations. The multiple stages of development were driven by three parallel processes, the first being the regulatory requirement for regular updates of the hazard and risk estimates for the Groningen field. This resulted in fully documented versions of the GMPM being generated at relatively short intervals, which brought both advantages and disadvantages. On the positive side, the incremental development provided opportunities for a rigorous review of each version of the GMPM and testing of models through the implementation in the hazard and risk calculations. On the negative side, the sprints to produce each version of the model, combined with the computational burden of the ground-motion simulations and site response analyses (see Section 5) meant that there was little opportunity to iterate on individual elements of the model as each complete version of the GMPM was generated. Moreover, two versions of the model were

affected by errors that arose due to the tight schedule: one version was influenced by a preliminary relationship between local and moment magnitude, which was subsequently revised, and another by errors in processing the large number of recordings from an earthquake that occurred just as the model-building process was starting.

The second driver for the generation of multiple versions of the GMPM was the growth of the database, both in terms of the number of ground-motion recordings available and the geotechnical characterisation of the recording stations. The ground-motion database expanded very considerably during the course of the model development, due to ongoing seismicity and the installation of new recording networks (see Section 3). Campaigns of in situ field measurements also led to most of the recording stations eventually having measured near-surface shearwave velocity, V_S, profiles.

The third driver of the model development was related to a progressive improvement of the modelling process to better capture the physical characteristics of the earthquakes, the wave propagation, and the dynamic response of the soft soil deposits. These refinements were prompted both by the insights of the authors and the suggestions and challenges of the review panel established to oversee the work (see Acknowledgements). For obvious reasons, the opportunities to refine the model were often closely linked to the availability of data.

Another factor in the development of the GMPMs, affecting the left-hand side of the equations rather than the functional form and parameters on the right, has been adapting to the evolution of the fragility functions defined for the building typologies encountered in the Groningen region (Crowley et al. 2017a, b; Crowley et al. 2019) and various potential applications of the model. At one time, this meant that the model included prediction of the duration of motion, but this is no longer required.

The GMPM development has also had to be compatible with the seismicity model that it links to the exposure and fragility models for the calculation of risk. The seismological model is based on local magnitude, M_L, as determined by the Dutch seismological service, KNMI. However, it has been demonstrated that for magnitudes larger than 2.5 (the lower limit for which the GMPM is applicable), M_L in Groningen can be considered equivalent, on average, to moment magnitude M (Dost et al. 2018, 2019).

The very first GMPM (version 0 or V0) was developed very rapidly and only predicted PGA and PGV. The model was essentially based on the equations of Akkar et al. (2014) developed for tectonic seismicity in the Mediterranean and Middle East regions, adjusted at smaller magnitudes (below 3.8 for PGV and below 4.2 for PGA) to match the small database of Groningen ground motions available when this work commenced (Bourne et al. 2015). At that time, estimates of V_{S30} (the time-average V_S over the uppermost 30 m) were not available for any of the recording stations; the model was applied assuming a field-average V_{S30} of 200 m/s, which has subsequently been confirmed as an accurate estimate.

The first complete GMPM (V1) was developed by inverting Fourier amplitude spectra of recorded surface motions to estimate the source ($\Delta\sigma$), path (Q), and average site parameters (amplification and site damping, κ_0). These parameters were then used in point-source stochastic simulations using SMSIM (Boore 2005) with different values of the stress parameter $\Delta\sigma$ in order to capture the epistemic uncertainty in extrapolating to larger magnitudes. While this model did reflect Groningen conditions, it had two important weaknesses in terms of the site response: the amplification corresponded to a network average (the network being located in the northern part of the field, where V_{S30} values are generally lower), and only linear site response was modelled, even up to large magnitudes. These shortcomings were addressed in the V2 GMPM, which established the basic framework used for all subsequent models. Fundamental to being able to implement this framework were the development of a field-wide V_S model (Kruiver et al. 2017a, b) and in situ measurements of V_S profiles at the recording stations (Noorlandt et al. 2018). In this GMPM, the surface motions were deconvolved to a buried rock horizon (at ~ 350 m depth), assuming linear site response because of the relatively low levels of motion. The same procedure as used for the V1 model was then applied to these rock motions to provide the inputs to stochastic simulations of motions at the rock horizon for a wide range of magnitudes. Frequency-dependent, non-linear amplification factors were then determined and assigned to zones, originally defined on the basis of near-surface geology, to transform the rock motions to the surface.

All subsequent versions of the model represented modifications to the V2 framework. In the V3 model, the reference rock horizon was moved to the base of the North Sea Supergroup at ~ 800 m depth, which is a more persistent and more pronounced impedance contrast (Bommer et al. 2017a). At this stage, the models were based on point-source simulations, despite the fact that the hazard and risk calculations considered a maximum magnitude, Mmax, of 6.5—determined on the basis of all the strain associated with full production of the gas reservoir being released seismically in a single event (Bourne et al. 2014). Epicentral distance, R_{epi}, was used as the distance metric because KNMI assigned a common focal depth of 3 km to all Groningen earthquakes. To compensate for the point-source approximation, a magnitude- and distance-dependent increase was imposed on the sigma value representing the aleatory variability associated with the predicted motions (Bommer et al. 2016). A workshop

dedicated to the estimation of Mmax for Groningen held in March 2016 resulted in a distribution of values peaking at 4.5, but with low-weighted upper tail exceeding magnitude 7 (Bommer and van Elk 2017). This prompted a move from V4 onwards to finite rupture simulations, using the software EXSIM (Motazedian and Atkinson 2005) as modified by Boore (2009). In conjunction with this change, the distance metric was changed from R_{epi} to rupture distance, R_{rup}, although for the small-magnitude events in the database, R_{Rup} was considered equivalent to hypocentral distance, R_{hyp}. At this point, the previously mentioned adjustment to the sigma values was dropped. Another change that was implemented in the V4 model was the inclusion of magnitude- and distance-dependence in the short-period linear site amplification factors, AFs (Stafford et al. 2017).

The framework of the V4 model has remained unchanged, with each subsequent version representing a refinement based on improved modelling, for example of the soil damping model (Ruigrok et al. 2022), and the continued growth of the ground-motion database. Up to the V5 model, the derivation used surface recordings from the B-network and geophone recordings at 200 m depth from the G-network (see Section 3), because measured V_S profiles were available at the former but not the latter, and the intention was to avoid the additional uncertainty in the transfer functions and AFs used to deconvolve the G-station recordings. However, doubts had arisen regarding the consistency of the surface and borehole recordings, possibly related to the operational issues with the borehole geophones, prompting the decision to use only surface accelerograms in the V6 model; this also meant that the deconvolution and forward modelling were along common paths. For the V7 model, measured V_S profiles had become available for nearly all the surface accelerographs in the G-network, removing entirely the original motivation for using borehole records. Additionally, the V7 model made use of more accurate depth determinations by Spetzler and Dost (2017), which reflected the convex shape of the reservoir over the field, in the calculation of R_{hyp}.

The V7 model presented herein represents the culmination of this evolutionary process. The V7 development benefited from an intervention by the international expert review panel, who counselled against running through yet another sprint to produce

another incremental modification of the V6 model. This resulted in the V6 model being used for another round of hazard and risk calculations, but this created the space for individual elements of the V7 model to be developed, reviewed, and refined prior to initiating the full model production process. Consequently, this is a model whose development has benefited from multiple iterations and enhancements and likely represents an asymptote in terms of potential improvements although we highlight some issues that would be worthy of additional investigation.

In this paper, we present the current ground-motion models for Groningen but do not make comparisons with the predictions from earlier versions of these models. Such comparisons are not straightforward in some cases because of changes of independent variables such as the distance metrics, but we believe that they are also of little value since each new model supersedes the previous development stages. Moreover, each model is judged on its own merit with respect to the data and the modelling decisions, not on whether it predicts higher or lower amplitudes of motion than the previous version. We begin by briefly summarising the ground-motion database and then we present an empirical model for PGV, which provides some useful insights into the nature of the recorded ground motions in the field, before summarising the current GMPM for seismic risk analysis in Groningen.

3 Groningen ground-motion database

The characteristics of the various seismic recording networks in and around the Groningen field are described by Dost et al. (2017) and Ntinalexis et al. (2019). The networks that provide the data used in the derivation of the GMPMs include the B-network, which comprises accelerographs installed by KNMI in houses and farm buildings mainly in the northern part of the field. Following the 2012 Huizinge earthquake, this network was expanded from 10 to 18 stations, and the instruments were upgraded to Kinemetrics Episensors; for reasons that will be made apparent in Section 4, the networks prior to and after the upgrade are referred to as B_old and B_new, respectively. The G-network, which is also operated by KNMI, was installed by NAM between 2014 and 2017, comprising 79 surface accelerographs (also

Episensors), 69 of which are co-located with a borehole instrumented with geophones at 50, 100, 150, and 200 m depths. The magnitude-distance distribution of the recordings, classified by recording network and by V_{S30}, is shown in Fig. 3. As can be appreciated, the stations are generally rather soft, with most records corresponding to V_{S30} values in the range from 160 to 260 m/s.

The records have all been processed uniformly following the procedure described by Edwards and Ntinalexis (2021). The database is described in greater detail by Ntinalexis et al. (2022), which also provides a link to a repository from which the entire collection of raw and processed accelerograms can be freely downloaded.

4 Empirical model for peak ground velocity

Several early versions of the GMPM included predictions for PGV, as well as response spectra accelerations and durations, for potential applications to risk analysis of some infrastructure lifelines, but this was discontinued since we were not aware of any such applications in practice. However, the need arose for

a PGV model to be used in the evaluation of damage claims, the cumulative value of which has reached unprecedented levels (Crowley et al. 2019; Bommer 2022). Since this model was to be applied only within the magnitude range of the data, an empirical ground-motion prediction equation (GMPE) was considered sufficient. For the derivation of this GMPE, a lower magnitude of M_L 1.8 was selected to cover the full range of felt events in the field. The recorded PGV values, grouped by magnitude ranges and plotted against hypocentral distance, are shown in Fig. 4. The largest PGV value in the database is 3.5 cm/s, which was recorded during the 2012 Huizinge earthquake.

The data in Fig. 4 display a distinct feature of the Groningen ground motions in terms of geometric spreading: rapid decay over short distances, a flattening between about 7 and 12 km, and more gradual decay at greater distances. This is consistent with the results of finite difference waveform modelling using a detailed 3D velocity model of the field (Edwards et al. 2019), which has been used to constrain the distances at which these transitions occur.

Modern GMPEs usually predict the geometric mean value of the two horizontal components of each accelerogram or other component definitions that

Fig. 3 Magnitude-distance distribution of the Groningen ground-motion database classified by the contributing accelerograph network (upper) and by the V_{S30} value at the recording station (lower)
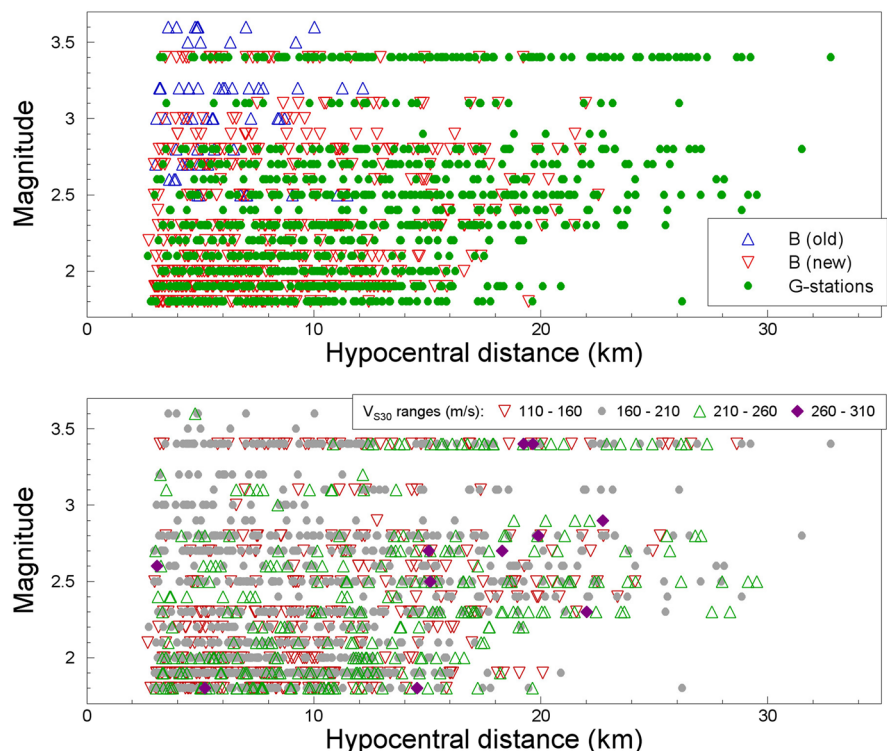
result in approximately the same values at most periods (e.g. Boore 2010). For the PGV GMPE for Groningen, however, coefficients were also derived for the larger horizontal components and maximum rotated. This component definition was chosen because it is consistent with the definition of the V_{top} parameter defined in Dutch guidelines for tolerable vibration thresholds; the model is presented only for the larger component.

The GMPE for the larger component obtained from regression on the empirical database is as follows:

$$\ln\left(PGV\right) = -3.3996 + 2.3258M + g(R) - 0.3295 \ \ln\left(\frac{V_{S30}}{200}\right) \tag{1}$$

with PGV in cm/s, M being local magnitude M_L, and V_{S30} is the harmonic average shear-wave velocity over the top 30 m (in m/s). The normalising V_{S30} value of 200 m/s was chosen on the basis of the approximate field average, but using another value would exert no influence on the predictions (it only changes the constant term). The distance term, R (in km), is an effective distance that accounts for magnitude-dependent near-source saturation effects, is a function of R_{hyp}, and is defined as follows:

$$R = \sqrt{R_{hyp}^2 + h(M)^2} \tag{2}$$

with the magnitude-dependent saturation term set equal to as follows:

$$h(M) = \exp(-3.4407 + 1.1513M) \tag{3}$$

In Eq. (3), the multiplier on magnitude is fixed to the constant value of 1.1513 so that the saturation distance scales in proportion to the expected rupture area, whereas the first coefficient is solved for in the regression. The distance dependence is defined by the following:

$$g(R) = -2.8522\ln(R) \ \ R \leq 7km \tag{4a}$$

$$g(R) = -2.8522\ln(7) - 1.0151\ln\left(\frac{R}{7}\right) \ \ 7 < R \leq 12 \ km \tag{4b}$$

$$g(R) = -2.8552\ln(7) - 1.0151\ln\left(\frac{12}{7}\right) - 2.1002\ln\left(\frac{R}{12}\right) \ R > 12 \ km \tag{4c}$$

The rapid decay of amplitude at short distances is interpreted to be the result of the refraction of the seismic waves by the high-velocity Zechstein salt layer (Kraaijpoel and Dost 2013).

The total variability in the predictions, σ, is decomposed into between-event (τ), site-to-site (ϕ_{S2S}), and within-event (ϕ_{ss}) standard deviations, all of which are related by the following expression (e.g. Al Atik et al. 2010):

$$\sigma = \sqrt{\tau^2 + \phi_{S2S}^2 + \phi_{ss}^2} \tag{5}$$

Fig. 4 As-recorded horizontal PGV values from the Groningen ground-motion database, grouped by magnitude, plotted against hypocentral distance
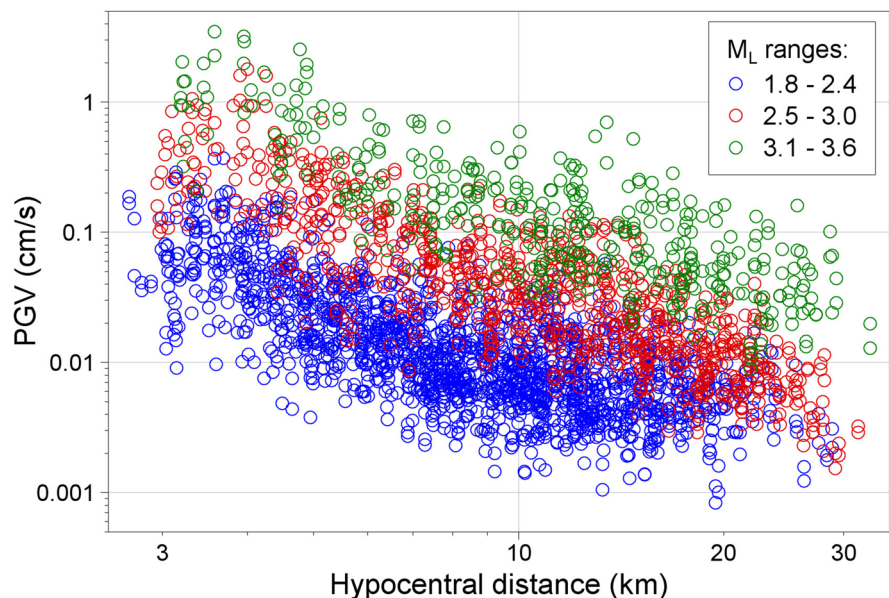
The estimates of these variance components as well as the coefficients of the GMPEs are also influenced by considering the uncertainty in magnitude determinations for each earthquake. The resulting values are summarised in Table 1.

An interesting observation that can be made is that the influence of V_{S30} is rather modest: decreasing the V_{S30} value from 260 m/s to 160 m/s results in only a 17% increase in the predicted median value. This is consistent with findings in other projects—including NGA-Sub (Parker and Stewart 2021) and NGA-East (Parker et al. 2019)—which find a flattening of the relative amplification as V_{S30} values become very low (< ~300 m/s). As a result of damage claims being submitted from a much larger area than that defined by the boundaries of the gas field, to facilitate the implementation of the PGV GMPE, a map of V_{S30}, defined at the level of 4-digit postcodes, has been generated (Fig. 5) following essentially the same procedures applied by Kruiver et al. (2017b) to construct the uppermost part of the field-wide V_S profiles.

Analysis of the residuals revealed that the models provide a good fit to the data, with no discernible trends with respect to magnitude, distance, or V_{S30} (Fig. 6). However, the residuals do show that the motions recorded at the B_new stations are, on average, lower than those from the G-network and the B_old stations. An apparent tendency for short-period motions—PGV in Groningen has been found to correlate well with the spectral acceleration at 0.2–0.3 s (Bommer et al. 2017b)—to be lower at the B-stations than the G-stations has been attributed by some researchers to soil-structure interaction (SSI) effects, which is an obvious candidate given that the B-network stations are installed in buildings

and the G-network stations are free-field accelerographs housed in small instrument shelters. The same researchers recommended that all the B-station recordings should therefore be removed from the database, which would mean the loss of many of the strongest motions and the majority of the near-source recordings of the larger events in the database (Fig. 3). Cavalieri et al. (2021), however, using advanced dynamic SSI analyses, demonstrated robustly that SSI effects do not explain any differences between B-network (not including those with basements) and G-network recordings in the short-period range. The same study showed that the most likely explanation is the presence of a layer of improved soil below the buildings housing the stations of the B-network, which are commonly created by pre-loading the soil with a layer of compacted sand prior to construction. No systematic correction for this effect can be made, however, since no information is available regarding the presence or absence of such soil layers at all the B-network stations. At the same time, it is noted that there are clear SSI effects at three of the B-network stations where the buildings include deep basements (BUHZ, BWIN, and BZN1), but corrections for the embedment effect at these stations are applied to all the recordings following the procedures recommended in NIST (2012). Ongoing investigations are underway in an attempt to identify and quantify the exact cause of the apparent differences between the B-station and G-station recordings, taking account of recent insights into the influence of instrument installation characteristics on the nature of recorded high-frequency motions (Hollender et al. 2020).

The interesting question that then arises is why this effect should manifest only in the upgraded B-stations (B_new) and not in B_old recordings. The recordings from B_old instruments, which operated on a triggering basis, were generally selected by KNMI for processing and distribution, and this manual process would naturally have favoured the stronger recordings, and lower amplitude motions will have been excluded. Analyses have indicated that the attenuating effect at the B-network stations being a function of amplitude and manifesting most consistently for lower levels of motion, although it should be clearly noted that no physical explanation for this observation has been put forward. The GeoSig accelerographs of the B_old stations displayed much higher noise levels than the new Episensor accelerographs (Ntinalexis et al. 2019).

Table 1 Variance components for the prediction of all horizontal component definitions of PGV

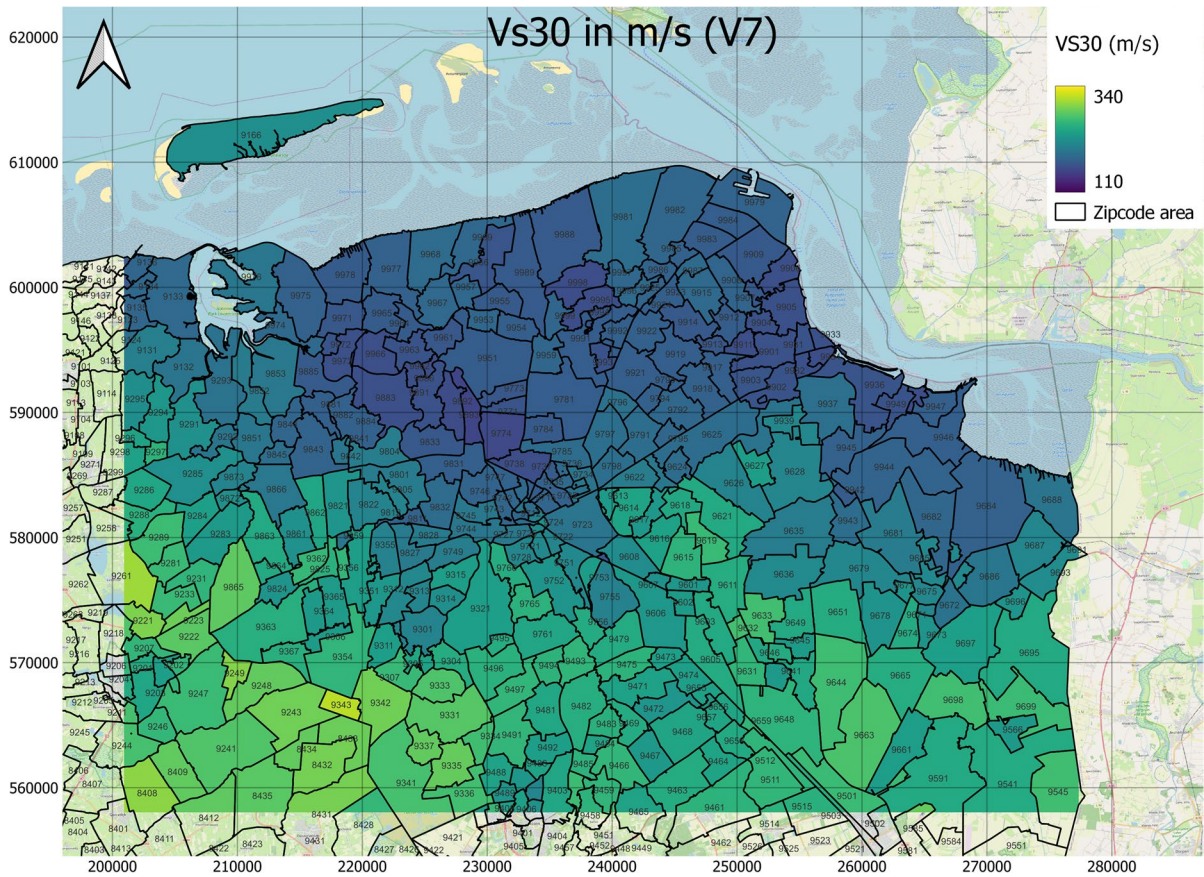| Equation	Component definition	τ	ϕ_{S2S}	ϕ_{ss}	σ
(1)–(4)	Geometric mean	0.2488	0.2420	0.4160	0.5418
	Larger	0.2448	0.2406	0.4569	0.5715
	Maximum rotated	0.2470	0.2442	0.4530	0.5708
(6)–(8)	Geometric mean	0.2509	0.2177	0.4160	0.5324
	Larger	0.2487	0.2165	0.4567	0.5634
	Maximum rotated	0.2521	0.2208	0.4530	0.5635

Fig. 5 Map of V_{S30} values at 4-digit postcode level for implementation of the PGV GMPE [coordinates in Dutch RD (Rijks-Driehoek) system. Dwelling mounds (*wierden*) were accounted for in the derivation of this map using the AAOP (anthropogenic material) stratigraphy for organic and clay material, and V_S measurements were performed at a number of dwelling mounds (Kruiver et al. 2022a)
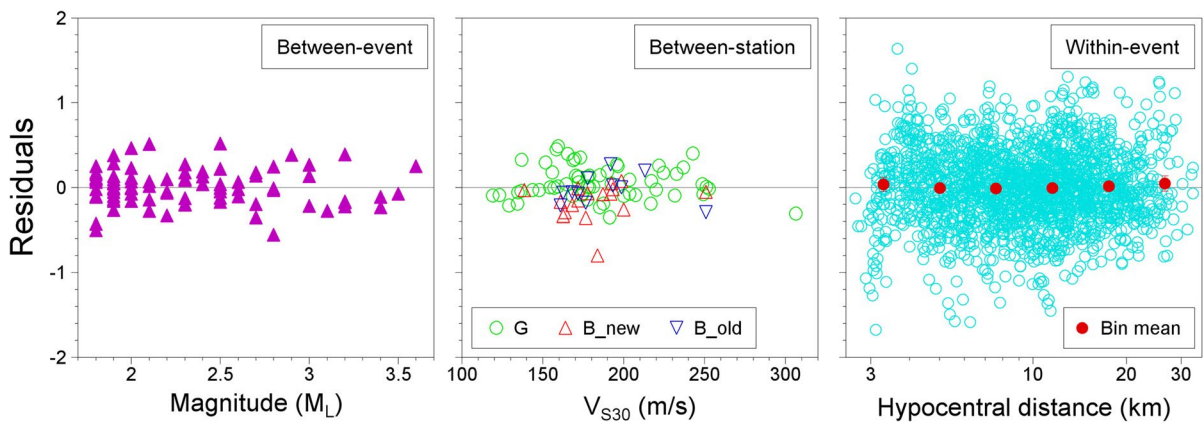

Fig. 6 Residuals of PGV (larger horizontal component) obtained from the network-independent model: inter-event residuals against magnitude, station-terms against V_{S30} (indicating network), and intra-event residuals against distance (circles and lines indicating mean residuals and 95% confidence intervals)

Consequently, an average effect of high-frequency suppression at the B-network stations may be genuine, but it could have been largely removed from the B_old recordings as a result of data selection procedures.

In view of the apparent influence of the recording network, an alternative form of Eq. (1) was also derived, including an additional term with a dummy variable F_{NB} that takes a value of 0 for B_new recordings and 1 otherwise:

$$\ln(PGV) = -3.584 + 2.3227M + g(R) - 0.3344 \ln\left(\frac{V_{S30}}{200}\right) + 0.2581F_{NB} \tag{6}$$

The near-source saturation term of Eq. (3) and the distance dependence defined in Eq. (4) become as follows:

$$h(M) = \exp(-3.4319 + 1.1513M) \tag{7}$$

$$g(R) = -2.8553 \ \ln(R) \ R \leq 7km \tag{8a}$$

$$g(R) = -2.8553 \ln(7) - 1.0282 \ln\left(\frac{R}{7}\right) \ 7 < R \leq 12 \ km \tag{8b}$$

$$g(R) = -2.8553 \ \ln(7) - 1.0282 \ln\left(\frac{12}{7}\right) - 2.1085 \ln\left(\frac{R}{12}\right) \ R > 12 \ km \tag{8c}$$

The inclusion of this term to distinguish the contributing accelerograph network leads to a small reduction in the total variability, as shown in Table 1. Figure 7 compares the median prediction from Eqs. (1) and (6), which shows the rather pronounced reduction in amplitudes at the B_new stations.

This raises the question of which equation should be used in applications. Since the objective is to estimate the level of shaking experienced by typical buildings in the region, the most appropriate model would be Eq. (6) with F_{NB} set to 0. However, there are two considerations that deter us from this recommendation, the first being that it is not known at what proportion of buildings in the Groningen region do the effects of attenuated high-frequency motions manifest. The current hypothesis is that the effect is due to improved soil layers below the foundations, but there are no data available to determine how pervasive this feature is among the entire building stock. The second consideration, which is not scientific but rather related to optics (and taking account of the regulatory environment and the nature of the scrutiny to

which the hazard and risk modelling is subjected), is that this would mean adopting the model yielding the lowest predictions, which would likely be treated with suspicion. Our recommendation, therefore, is to use the model derived from all the available recordings, combining the free-field G-stations and the B-stations within buildings, namely Eq. (1). The implicit assumption in this choice is that collectively, the recordings obtained from the stations of both networks approximate the distribution of buildings with and without the high-frequency attenuation effect.

Additional details on the derivation of the PGV models are presented in Bommer et al. (2021), where the coefficients for the prediction of other horizontal component definitions can also be found.

A final point that can be made here is that the variability components presented in Table 1 allow the event term to be calculated for any earthquake using the recordings that become available on the KNMI portal soon after each earthquake. The event term can then be subtracted from the constant term in the equation, and predicted motions can be estimated sampling only from the within-event variability.

5 Models for the prediction of response spectral accelerations

The GMPM developed for seismic risk analysis predicts 5%-damped ordinates of pseudo-spectral acceleration, Sa(T), at 10 oscillator periods, T (0.01, 0.1, 0.2, 0.3, 0.4, 0.5, 0.6, 0.7, 0.85, and 1.0 s); the fragility functions for buildings in the Groningen exposure model are defined in terms of the geometric mean value of Sa over these periods. The model is developed to predict the geometric mean horizontal component of motion, for application to hazard assessments, but the appropriate definition for the risk analyses is the arbitrary horizontal component of motion, which requires an adjustment to the standard deviation to account for the component-to-component variability (Baker and Cornell 2006). The GMPM needs to be applicable over the full range of magnitudes considered in the risk calculations, with a lower limit set at 2.5 and upper limit at 7.25, also accounting for the uncertainty associated with this large extrapolation

Fig. 7 Predicted median PGV values against R_{hyp} for three magnitudes from the models with and without the term to distinguish the contributing accelerograph network
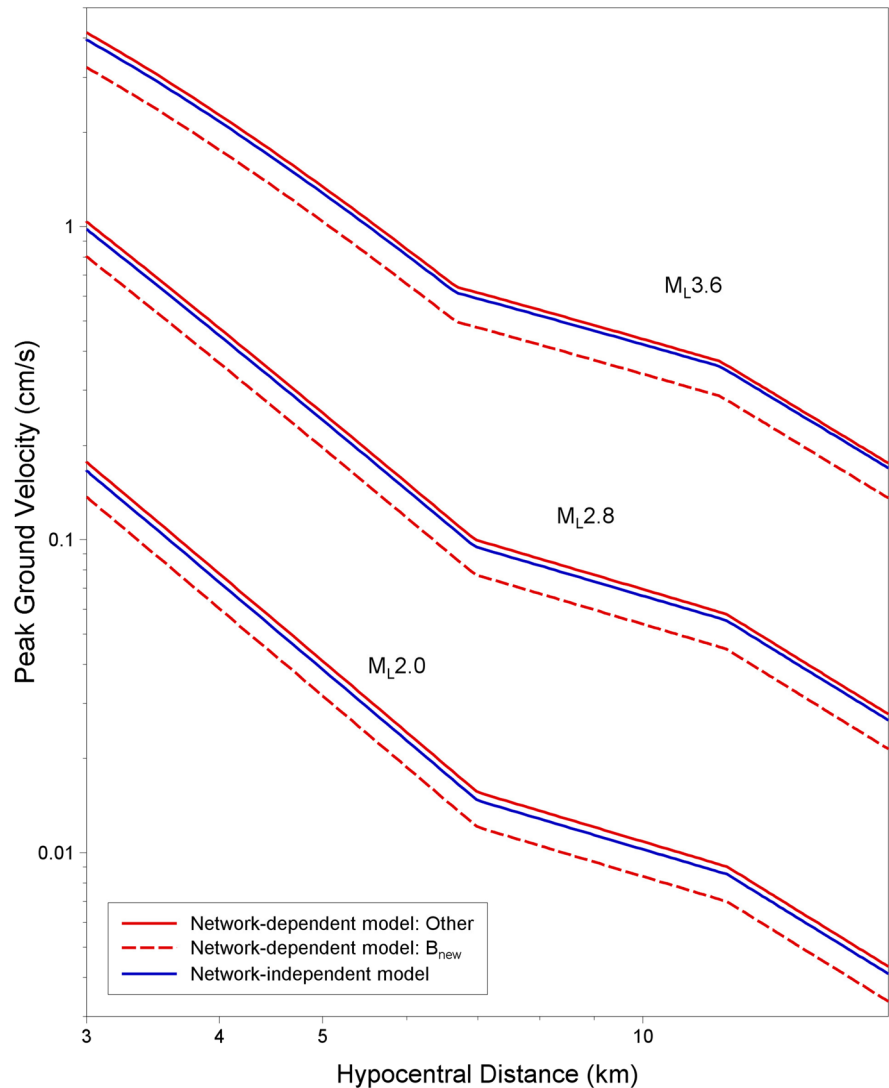
beyond the upper limit of the data. As a result of considering much stronger earthquake scenarios than those that have occurred in the field, the GMPM was also required to consider the non-linear site response of the soft soil deposits that cover most of the region of interest.

As with the PGV predictions, our choice was to use all the available ground-motion data, regardless of the network from which it was derived, provided there was a measured V_S profile for the recording station. This is a less critical choice than in the derivation of the empirical PGV model since the model is not obtained by direct regression on the recordings, but the data are used in the estimation of the variance components.

5.1 Model overview

The overall scheme for the derivation of the V7 GMM is illustrated schematically in Fig. 8. The essential elements of the GMM are equations to predict Sa at the NS_B reference rock horizon and non-linear amplification factors (AF) that transform the NS_B motions to surface accelerations. The derivation of the model for the prediction of Sa at the NS_B horizon and of the AFs is explained in Sections 5.2 and 5.3, respectively, including the quantification of both aleatory variability and epistemic uncertainty in both parts of the model. The basic framework is presented below, but the reader interested in greater detail regarding the model derivation can refer to Bommer et al. (2022).

6 Reference rock model

Using the V_S profiles down to the NS_B horizon at each recording station, together with the damping profiles (Ruigrok et al. 2022), transfer functions (TFs) are developed to deconvolve the Fourier amplitude spectra (FAS) to the reference rock horizon; here, as in all the site response modelling, we make the standard assumption of vertically propagating waves. The high-frequency damping parameter κ is estimated using the method of Anderson and Hough (1984) and then the FAS are inverted to estimate the geometric spreading coefficients (using the hinge distances constrained by finite difference simulations of the wave propagation), the average quality factor Q (using a layered Q model), and the stress parameter $\Delta\sigma$. Due to the inevitable trade-offs among these parameters, there are many combinations that are found to be consistent with the FAS. The next step is to calculate scenario-dependent AFs using the site profiles and the available recordings

from each station. These AFs are then used to deconvolve the Sa to the NS_B horizon. With the attenuation functions fixed (R^{-x} and Q), point-source simulations (using SMSIM) are used to generate response spectra at the NS_B horizon for the M-R pairs of the recordings. The average bias between the predictions and the deconvolved response spectra, averaged over the 10 target oscillator periods, is calculated to determine the optimal combination of $\Delta\sigma$ and κ to match the recorded motions (black cross in left-hand panel of Fig. 9). To capture the epistemic uncertainty, two alternative $\Delta\sigma$-κ combinations that also lead to low bias (blue crosses in left-hand panel of Fig. 9) are also selected. The central model is defined by $\Delta\sigma = 22$ bars and κ equal to 0.002 s; the upper and lower values of the stress parameter are 33 and 15 bars.

On the basis of conclusions from the expert panel appointed to develop the Mmax distribution for Groningen (Bommer and van Elk 2017), any earthquakes of magnitude greater than 5 would be assumed to be
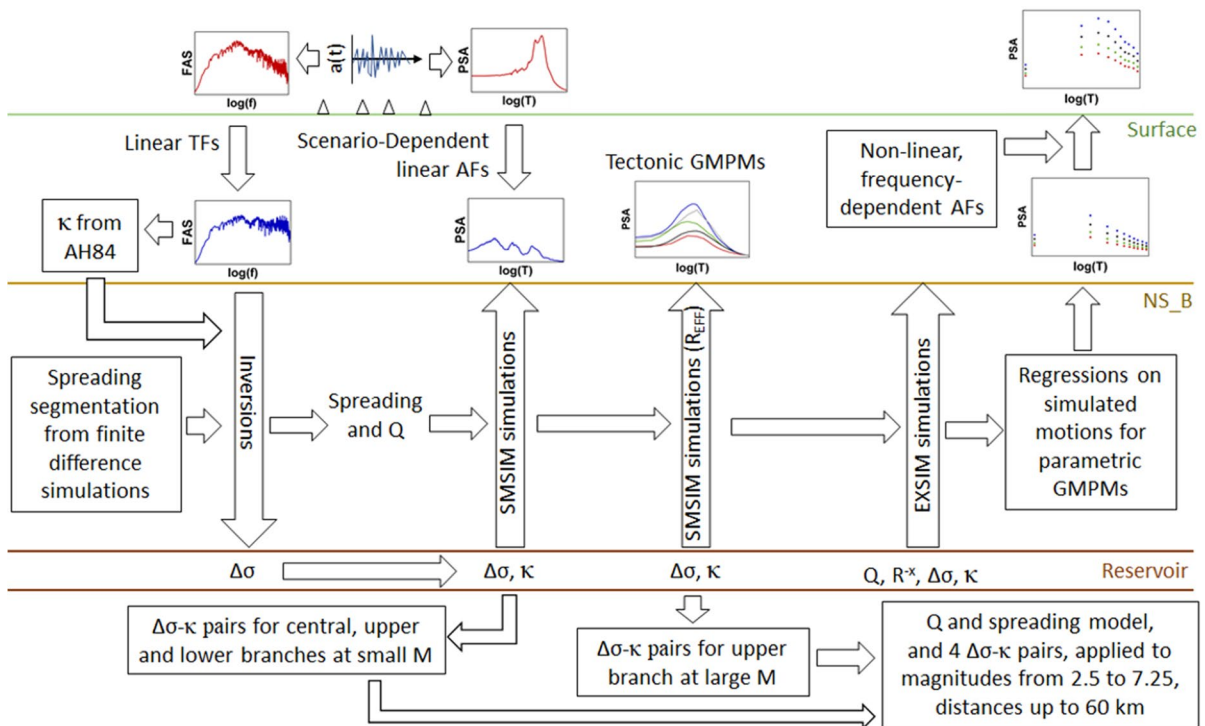

Fig. 8 Schematic illustration of the process to derive the V7 GMM. TF is transfer function, AF is amplification factor, and R^{-x} represents geometric spreading with R being distance. AH84 Anderson and Hough (1984) to estimate κ. The triangles represent surface accelerograph stations of both the B- and G-networks. R_{EFF} is a magnitude-dependent effective distance (Boore 2009)

triggered events that rupture largely outside of the reservoir (which would imply rupture propagation downwards into the Carboniferous since faults would not rupture the overlying salt deposits). In order to create a branch of the logic-tree to accommodate such tectonic earthquakes (even though large ruptures initiating at 3 km depth and propagating downwards would be unusual), values of the stress parameter were determined to match, over the 10 target periods, Sa predicted from tectonic GMPMs. Using the models of Abrahamson et al. (2014), Akkar et al. (2014), Bindi et al. (2014), Boore et al. (2014), Campbell and Bozorgnia (2014), and Chiou and Youngs (2014), median Sa values were predicted at the NS_B using $V_{S30} = 1400$ m/s for magnitudes 5, 5.5 and, 6 for logarithmically spaced distances up to 20 km. Simulations were then performed for the same M-R combinations using the central value of κ to explore the $\Delta\sigma$ value that best matched the spectra from the tectonic earthquakes. For efficiency, these simulations were performed with SMSIM using the magnitude-dependent effective distance to account for finite-source effects, which has been shown to be reasonable approximation (Boore 2009). The optimal value of $\Delta\sigma$, giving the smallest bias in the predicted spectra at NS_B, was found to be 50 bars (see right-hand panel of Fig. 9).

To model the epistemic uncertainty in the predictions, a logic tree is established with three branches for the value of the stress parameter in the magnitude range of the data (i.e. 2.5 to 3.6), with the dominant weight (0.6) on the central branch and weights of 0.2 on the upper and lower alternative branches. The range of epistemic uncertainty for the predictions at magnitudes of 5 and greater must be large by virtue of the extrapolation beyond the data and the fact that nothing is known about the fault ruptures that would be associated with such events. The end members were therefore defined by maintaining the lowest stress parameter branch constant across the magnitude range, at the lower end, and converging to the branch calibrated to tectonic GMPMs at the upper end. To adequately cover the space between these two limits, the central branch bifurcates for magnitudes above 3.6 and converges to branches that are equally spaced in terms of $\log(\Delta\sigma)$ for magnitudes of 5 and greater (Fig. 10, upper). In the large magnitude range, the lowest branch is considered feasible but somewhat unlikely, so its weight is reduced to 0.1, and the distribution of weights becomes skewed towards the higher branches; consequently, the branch weights are not constant but vary with magnitude (Fig. 10, lower).

The four values of $\Delta\sigma$, each coupled with a value of κ_0 at the NS_B, are used to model the sub-events in finite fault simulations using EXSIM, which are performed for events covering the full magnitude range in increments of 0.25 units. For each earthquake, a fault rupture is defined with a dip consistent with the observed geometry of faults in the field and dimensions calculated from Wells and Coppersmith (1994). The hypocentre is located randomly along the strike
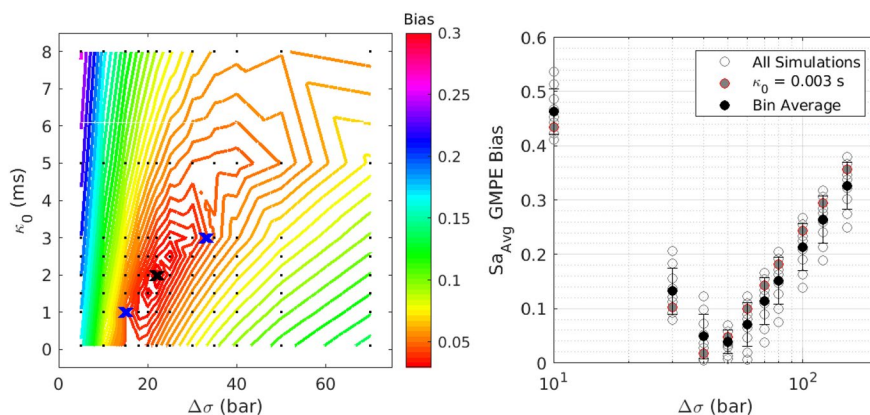

Fig. 9 Left: bias of predicted Sa at the NS_B with respect to the recorded Sa deconvolved to this horizon, as a function of kappa and the stress parameter, the black cross indicating the best-fit solution and the blue crosses alternative values for the upper and lower branches. Right: similar plot for the bias with respect to predicted Sa from several tectonic GMPMs as a function of the stress parameter with kappa fixed to the central value

of the fault along the top of the rupture (i.e. within the reservoir) and the fault propagates downwards (Fig. 11). Waveforms are generated at receiver locations directly above the top of the rupture and at logarithmically spaced distances out to 60 km at various azimuths, with additional recording stations situated at the hinge distances that define the different segments of geometric spreading. Response spectral accelerations are calculated from the waveforms to create a suite of simulated ground-motions for all magnitude and distance combinations.

One important feature of the simulations to be noted is that although the target is the NS_B at 800 m depth, the path is extended to the surface with infinite Q (i.e. no damping) in the layers above the reference rock horizon. The motivation for this choice is the rather unusual situation where a significant

proportion of the travel path is modelled through site response analyses, which assume 1D vertical wave propagation and therefore do not account for geometrical spreading in the uppermost portion of the travel path. This was considered to be preferable to the alternative of only propagating the motions to the NS_B horizon, which would ignore the geometric spreading over about one-quarter of the total travel path to the surface (for epicentral motions) and also result in higher motions at the NS_B, leading to more nonlinear response in the overlying layers.

To facilitate the implementation of the ground-motion predictions, parametric equations are derived through regression on the spectral accelerations generated from the simulations. The equations are a function only of magnitude and distance, but the functional form is somewhat

Fig. 10 Logic tree for the median motions at NS_B showing the values of stress parameter (upper) and the associated branch weights (lower) as these vary with magnitude
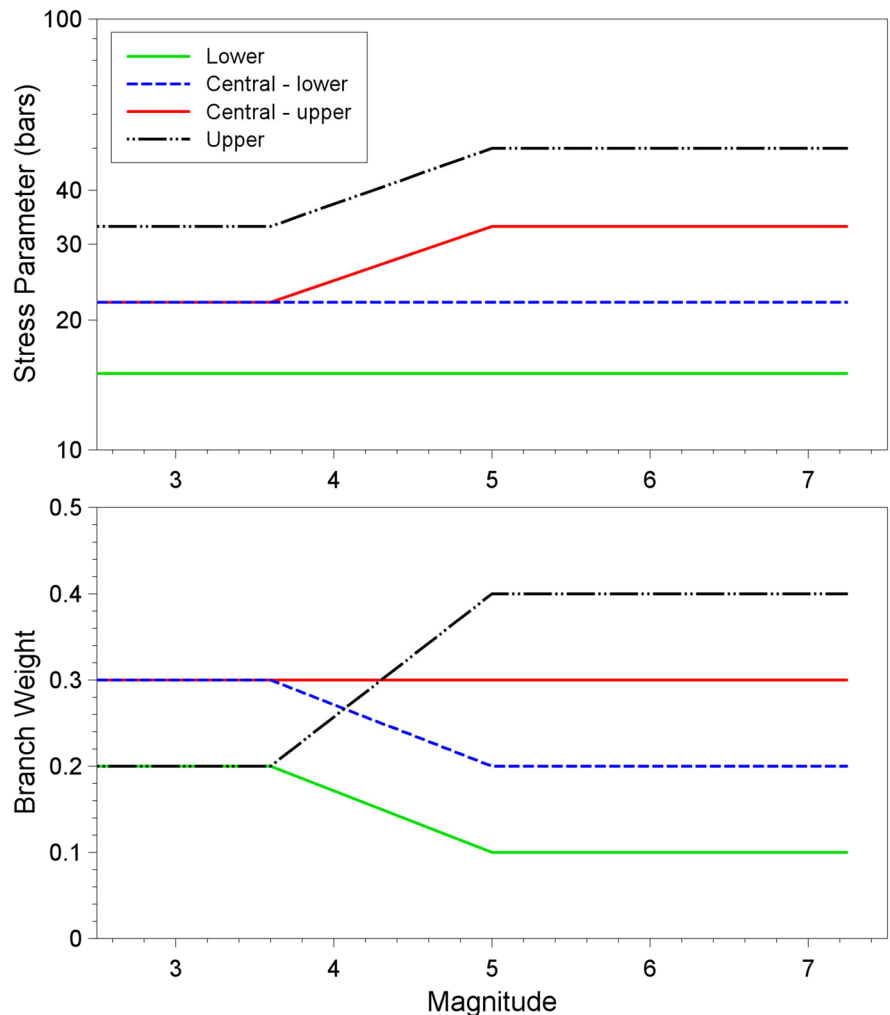
complex in order to capture the non-linear magnitude scaling over the range of magnitudes for which the model is applicable and the segmented geometric spreading. In contrast to the PGV models, the geometrical spreading is also magnitude dependent. The overall form of the equation for the prediction of Sa at the NS_B horizon is as follows:

$$\ln[Sa(\boldsymbol{M}, R_{rup}; T)] = g_{src}(\boldsymbol{M}; T) + g_{path}(R_{rup}, \boldsymbol{M}; T) \tag{9}$$

in which the source-related function is as follows:

$$g_{src}(\boldsymbol{M}; T) = \begin{cases} m_0(T) + m_1(T)(\boldsymbol{M} - M_m) + m_2(T)(\boldsymbol{M} - M_m)^2 & \text{for } \boldsymbol{M} < M_m \\ m_0(T) + m_3(T)(\boldsymbol{M} - M_m) + m_4(T)(\boldsymbol{M} - M_m)^2 & \text{for } \boldsymbol{M} \geq M_m \end{cases} \tag{10}$$

The hinge magnitude separating the two quadratic magnitude scaling functions, M_m, is 4.75. The path-related function is as follows:

$$\begin{aligned} g_{path}(R_{rup}, M; T) = {} & r_0(M; T) \ln\left(\frac{\max\left[\min\left(R_{rup}, R_{h,1}\right), R_{h,0}\right]}{R_{h,0}}\right) \\ & + r_1(M; T) \ln\left(\frac{\max\left[\min\left(R_{rup}, R_{h,2}\right), R_{h,1}\right]}{R_{h,1}}\right) \\ & + r_2(M; T) \ln\left(\frac{\max\left[\min\left(R_{rup}, R_{h,3}\right), R_{h,2}\right]}{R_{h,2}}\right) \\ & + r_3(M; T) \ln\left[\frac{\max\left(R_{rup}, R_{h,3}\right)}{R_{h,3}}\right] \end{aligned} \tag{11}$$

Consistent with Eq. (8), the hinge distances separating different rates of spreading are defined as $R_{h,0} = 3$ km, $R_{h,1} = 7$ km, $R_{h,2} = 12$ km, and $R_{h,3} = 25$ km, while the rates r_0, r_1, r_2, r_3 are defined by the expressions in Eqs. (12) to (15):

$$r_0(\boldsymbol{M}; T) = \begin{cases} r_{0,a}(T) + r_{0,b}(T)(\boldsymbol{M} - M_r) & \text{for } \boldsymbol{M} \leq M_r \\ r_{0,a}(T) + r_{0,c}(T)\tanh\left[r_{0,d}(\boldsymbol{M} - M_r)\right] & \text{for } \boldsymbol{M} > M_r \end{cases} \tag{12}$$

$$r_1(\boldsymbol{M}; T) = \begin{cases} r_{1,a}(T) + r_{1,b}(T)(\boldsymbol{M} - M_r) & \text{for } T \leq 0.2 \text{ s, and } \boldsymbol{M} \leq M_r \\ r_{1,a}(T) + r_{1,c}(T)\tanh\left[r_{1,d}(\boldsymbol{M} - M_r)\right] & \text{for } T \leq 0.2 \text{ s, and } \boldsymbol{M} > M_r \\ r_{1,a}(T) + r_{1,b}(T)(\boldsymbol{M} - M_r) & \text{for } T > 0.2s \end{cases} \tag{13}$$

$$r_2(\boldsymbol{M}; T) = \begin{cases} r_{2,a}(T) + r_{2,b}(T)(\boldsymbol{M} - M_r) & \text{for } T \leq 0.5 \text{ s, and } \boldsymbol{M} \leq M_r \\ r_{2,a}(T) + r_{2,c}(T)\tanh\left[r_{2,d}(\boldsymbol{M} - M_r)\right] & \text{for } T \leq 0.5 \text{ s, and } \boldsymbol{M} > M_r \\ r_{2,a}(T) + r_{2,b}(T)(\boldsymbol{M} - M_r) & \text{for } T > 0.5s \end{cases} \tag{14}$$

$$r_3(\boldsymbol{M}; T) = \begin{cases} r_{3,a}(T) + r_{3,b}(T)(\boldsymbol{M} - M_r) & \text{for } \boldsymbol{M} \leq M_r \\ r_{3,a}(T) + r_{3,c}(T)\tanh\left[r_{3,d}(\boldsymbol{M} - M_r)\right] & \text{for } \boldsymbol{M} > M_r \end{cases} \tag{15}$$

These equations require the determination of up to 21 coefficients at the shortest periods, with slightly fewer being required at longer periods. However, we also have a very large dataset of EXSIM simulations
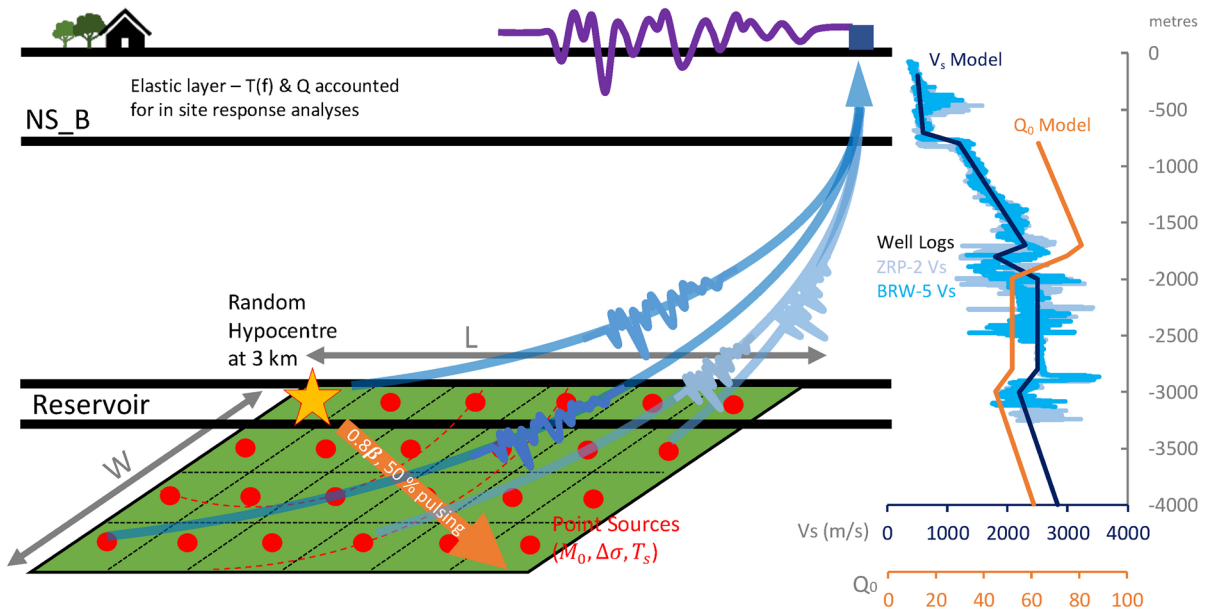

Fig. 11 Schematic illustration of the forward simulations using EXSIM. M_0 is the seismic moment and T_S the rise time, which is taken as the reciprocal of the corner frequency; β is the shear-wave velocity and the rupture propagates at 0.8β; the right-hand shows the V_S and Q profiles down to 4 km, including the top of the Carboniferous; and W and L are the width and length, respectively, of the fault rupture

and empirical observations that provide an excellent constraint on the initial estimates of these coefficients. Examples of the predicted median Sa values from the four models that occupy the logic-tree branches are plotted in Fig. 12. The plots clearly show the strong magnitude dependence of the geometric spreading and the increase of epistemic uncertainty with increasing magnitude.

The aleatory variability is defined in the same way as for the PGV model (Eq. (5)), but in this case, the site-to-site variability is accounted for in the AFs determined from site response analyses for the overlying layers (see Section 5.3); hence, the variability at the NS_B horizon is given by the single-station sigma (Atkinson 2006) defined by the following:

$$\sigma_{ss} = \sqrt{\tau^2 + \phi_{ss}^2} \tag{16}$$

The model for ϕ_{SS}^2 is based upon work originally conducted by Rodriguez-Marek et al. (2013) that was subsequently updated by Al Atik (2015). The approach assumes that the variance ϕ_{SS}^2 is χ^2-distributed and to select quantiles of this χ^2-distribution as discrete logic-tree nodes, two equally weighted branches are adopted corresponding to the 16th and 84th percentiles of the distribution. The within-event variability is independent of magnitude and distance but varies with the oscillator period. The between-event variability is determined from the residuals of the Sa of the ground-motion records deconvolved to the NS_B with respect to the median models, accounting for the uncertainty in the magnitude estimate for each earthquake. The results are found to display a small dependence on period, but this is sufficiently small to be ignored; hence, a constant value was adopted for the entire period range (Fig. 13). The final model is based on three branches that correspond to the 5th, 50th, and 95th percentiles, with weights assigned based on standard discrete approximations. The logic tree for the variance components therefore has two nodes with three (τ) and two branches (ϕ_{SS}), respectively; values of single-station intra-event have been found to be relatively stable globally, whereas there is little or constraint—and hence greater uncertainty—on the inter-event variability in the model at larger magnitudes. These six branch combinations are each combined with each of the four branches for the median predictions, leading to a total of 24

separate predictions for each realisation of the NS_B motions.

For risk calculations, as noted previously, it is necessary to transform the predicted spectral accelerations from the geometric mean component to the arbitrary component, for which the component-to-component variability σ_{c2c} must be added to the variance. A magnitude- and distance-dependent model for σ_{c2c} has been derived from the highly polarised Groningen data (Stafford et al. 2019); the model is calibrated to converge to the values found by Campbell and Bozorgnia (2007) from tectonic earthquake recordings for distances of 25 km and greater and for magnitude of 5.6 and larger. To correctly calculate the average spectral acceleration required as input to the fragility functions, the period-to-period correlation structure of Baker and Jayaram (2008), which has been found to be consistent with the Groningen data (computing inter-period correlations for residuals at the NS_B horizon, which is equivalent to looking at the correlation structure of the surface motions since deterministic site response effects are used to map from the surface to NS_B), is imposed.

6.1 Site response model

The V_S and lithological model for the entire study region—which is defined by the boundary of the gas field plus a 5 km buffer onshore—is developed in the form of voxel stacks of area 100×100 m that extend from the ground surface to the NS_B horizon. The construction of the profiles is described in Kruiver et al. (2017a, b), with some minor modifications and refinements that have been made subsequently. The modulus damping and reduction (MRD) curves of Darendeli (2001) and Menq (2003) are selected for clays and sands, respectively, whereas the MRD curves derived by Zwanenburg et al. (2020) from tests of local soil samples are applied to the Holland peat; for older and more consolidated deposits at depths greater than ~350 m (the Lower North Sea formation), a linear response is assumed. While this is perhaps an unusually large depth over which to assume a nonlinear response, the soft nature of the Groningen soils means that large strains are possible for some cases, even at considerable depths. The site response analyses are performed using the STRATA program by Kottke and Rathje (2008) using the random vibration theory (RVT; Rathje and Ozbey 2006) option, which
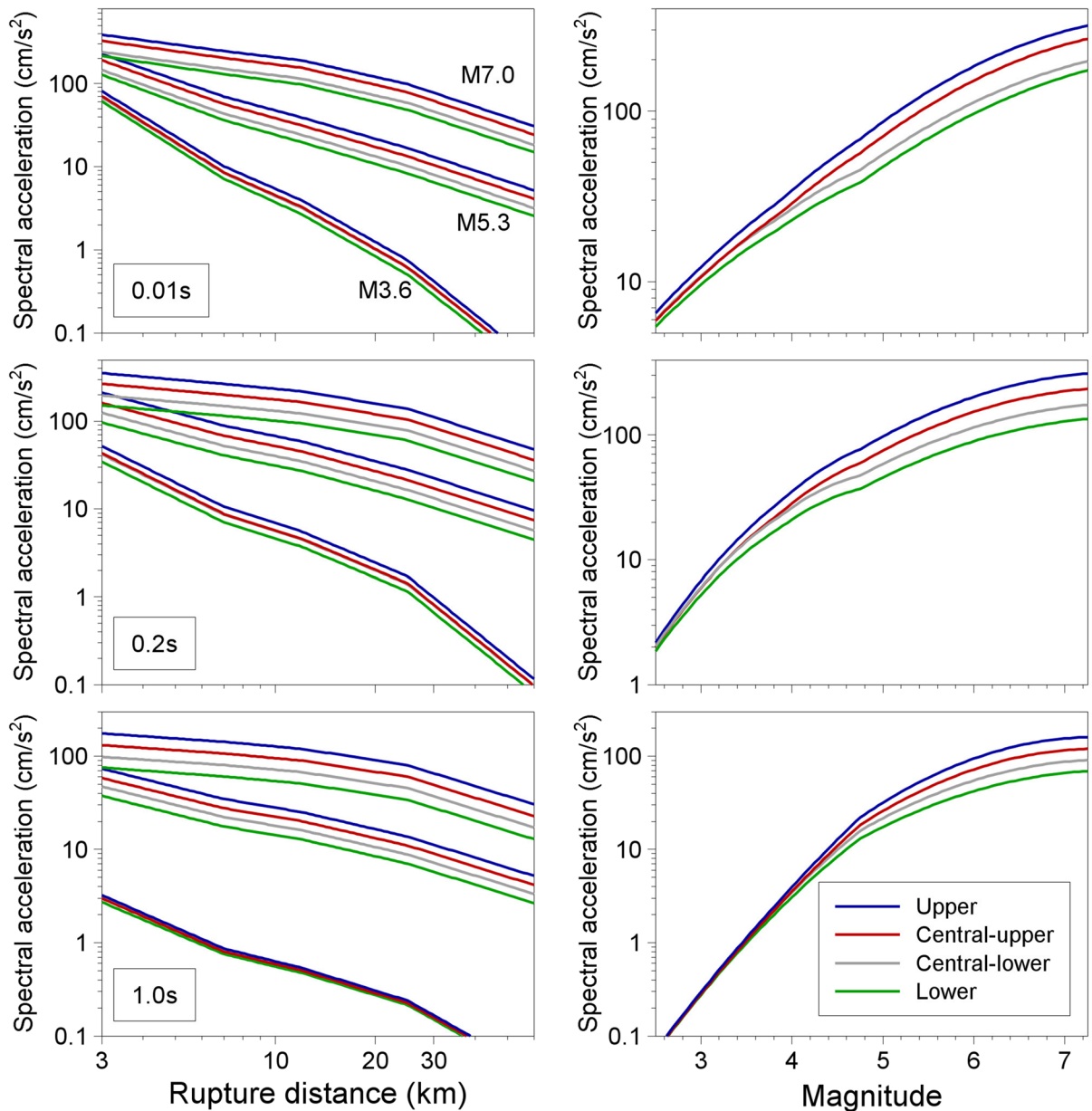
Fig. 12 Predicted median rock spectral accelerations at periods of 0.01 s (top), 0.2 s (middle), and 1.0 s (bottom) from the four models on the logic tree for various magnitudes as a function of distance (left) and as a function of magnitude for $R_{rup} = 5$ km (right)

requires input in the form of FAS at the NS_B, which are obtained from the simulations. Although refinements have been made to the model and to the procedures, the process for obtaining the AFs is essentially as described by Rodriguez-Marek et al. (2017).

The amplification factors are grouped into 160 zones over the field (Fig. 14). The zonation was originally defined on the basis of near-surface

geology (Kruiver et al. 2017a) and subsequently modified to achieve a high degree of consistency of the AFs within each zone (Rodriguez-Marek et al. 2017). These modifications to the zonation boundaries have been relatively minor, showing the geological zonation was a surprisingly good surrogate for site amplification, and in the transition from the V6 to V7 GMPM, it has remained unchanged.

Fig. 13 Calculated values of the inter-event variability at the 10 target periods from the four models, shown together with the three-branch model for τ (solid and dashed black lines). Also shown are the lines (in green) from the equivalent NGA-West2 model (Al Atik 2015), which confirms that the values are appropriate for the larger magnitude earthquakes
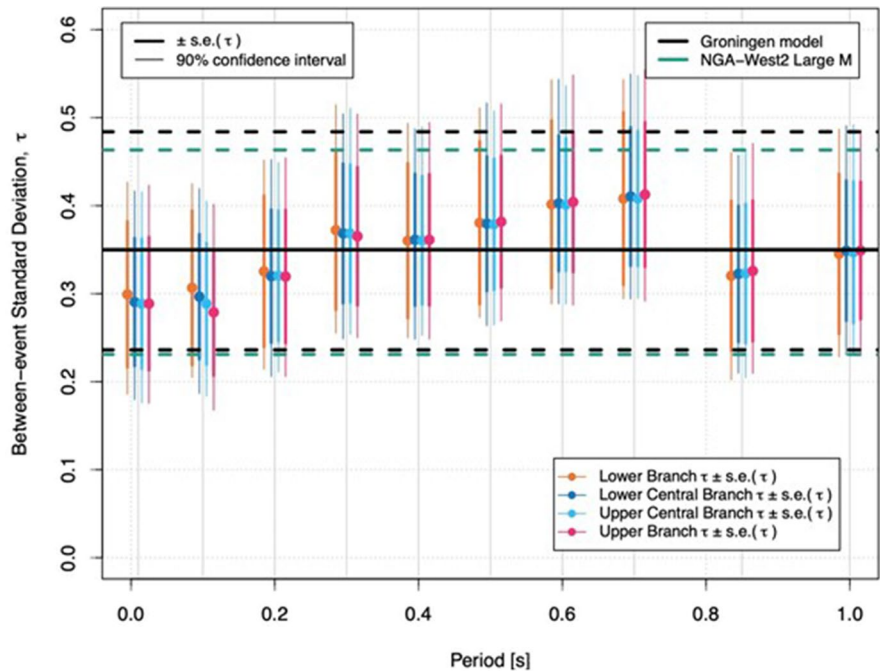
Figure 15 shows the AFs obtained from the site response analyses at nine oscillator periods for Zone 1801, which has an average V_{S30} very close to the average over the entire field. The plots show that the response is highly non-linear, and for short oscillator periods, the linear response is also strongly dependent on magnitude (and, to a lesser extent, on distance).

The computed AFs are used to derive an intensity and scenario (magnitude and distance) dependent model. The selected model is given by (Stewart et al. 2014):

$$\ln(AF) = f_1^* + f_2 \ln\left(\frac{Sa_{NS\_B,g} + f_3}{f_3}\right) + \varepsilon \sigma_{lnAF} \qquad (17)$$

where $Sa_{NS\_B,g}$ is the spectral acceleration at the NS_B horizon and is given in units of g (the acceleration of gravity), f_2 and f_3 are model parameters, ε is a standard normal random variable, σ_{lnAF} is a parameter that represents the standard deviation of the data with respect to the median prediction of the model. The parameter f_1^* is magnitude-and distance-dependent and is given by the following:

$$
\begin{aligned}
f_1^* = & \left[a_0 + a_1 \ln(R)\right] + \left[b_0 + b_1 \ln(R)\right]\left[\min\left(M, M_{ref1}\right) - M_{ref1}\right] \\
& + a_2 \left[\ln(R) - \ln\left(R_{ref}\right)\right]^2 + b_2 \left[\min\left(M, M_{ref1}\right) - M_{ref2}\right]^2 \\
& + a_3 \left[\max\left(M, M_{ref1}\right) - M_{ref1}\right]
\end{aligned}
\qquad (18)
$$

where M is magnitude, R is closest distance, a_i, b_i, M_{ref2}, and R_{ref} are model parameters, and M_{ref1} is given by the following:

$$
M_{ref1} = \begin{cases}
M_a & \text{for } R < 3\,\text{km} \\
M_a + \frac{\ln(R) - \ln(3)}{\ln(60) - \ln(3)}\left(M_b - M_a\right) & \text{for } 3\,\text{km} \le R \le 60\,\text{km} \\
M_b & \text{for } R > 60\,\text{km}
\end{cases}
\qquad (19)
$$

where M_a and M_b are model parameters. Equation (19) captures a quadratic dependence of the linear AFs with respect to magnitude and distance for magnitudes lower than M_{ref1}. For magnitudes greater than M_{ref1}, the model has a linear magnitude dependence. As with the reference rock prediction equations, the model is applicable for magnitudes up to 7.25 and distances up to 60 km. To avoid unrealistic AF values outside the range of Sa_{NS_B} represented by the input motions, for each zone and for each period, a minimum and maximum AF are also imposed. The resulting AFs for all the zones are shown in Fig. 16.

The standard deviation σ_{lnAF} is allowed to vary with the input spectral acceleration (i.e. a heteroskedastic model) and is fitted using a trilinear function given by the following:

$$\sigma_{lnAF} = \begin{cases} \sigma_{lnAF,\text{low}} & \text{for } Sa_{N\_B,g} < x_l \\ \sigma_{lnAF,\text{low}} + \left(\sigma_{lnAF,\text{high}} - _{lnAF,\text{low}}\right)\frac{\ln(Sa_{NB\_B,g}) - \ln(x_l)}{\ln(x_h) - \ln(x_l)} & \text{for } x_l \leq Sa_{NS\_B,g} \leq x_h \\ \sigma_{lnAF,\text{high}} & \text{for } Sa_{NS\_B,g} > x_h \end{cases} \tag{20}$$

where σ_{low}, σ_{high}, x_l, and x_h are model parameters. This represents the variability across the voxel stacks within a zone and across the range of input motions,

but the full site-to-site variability also needs to account for the additional uncertainty due to uncertainty in the MRD curves, which were not varied

Fig. 14 Zonation of the field and surrounding area for AFs. The colours denote soil profiles with typical succession of formations shown in the legend. Abbreviations are standard GeoTOP codes, except for 'pleis-var', which means a variety of Pleistocene deposits
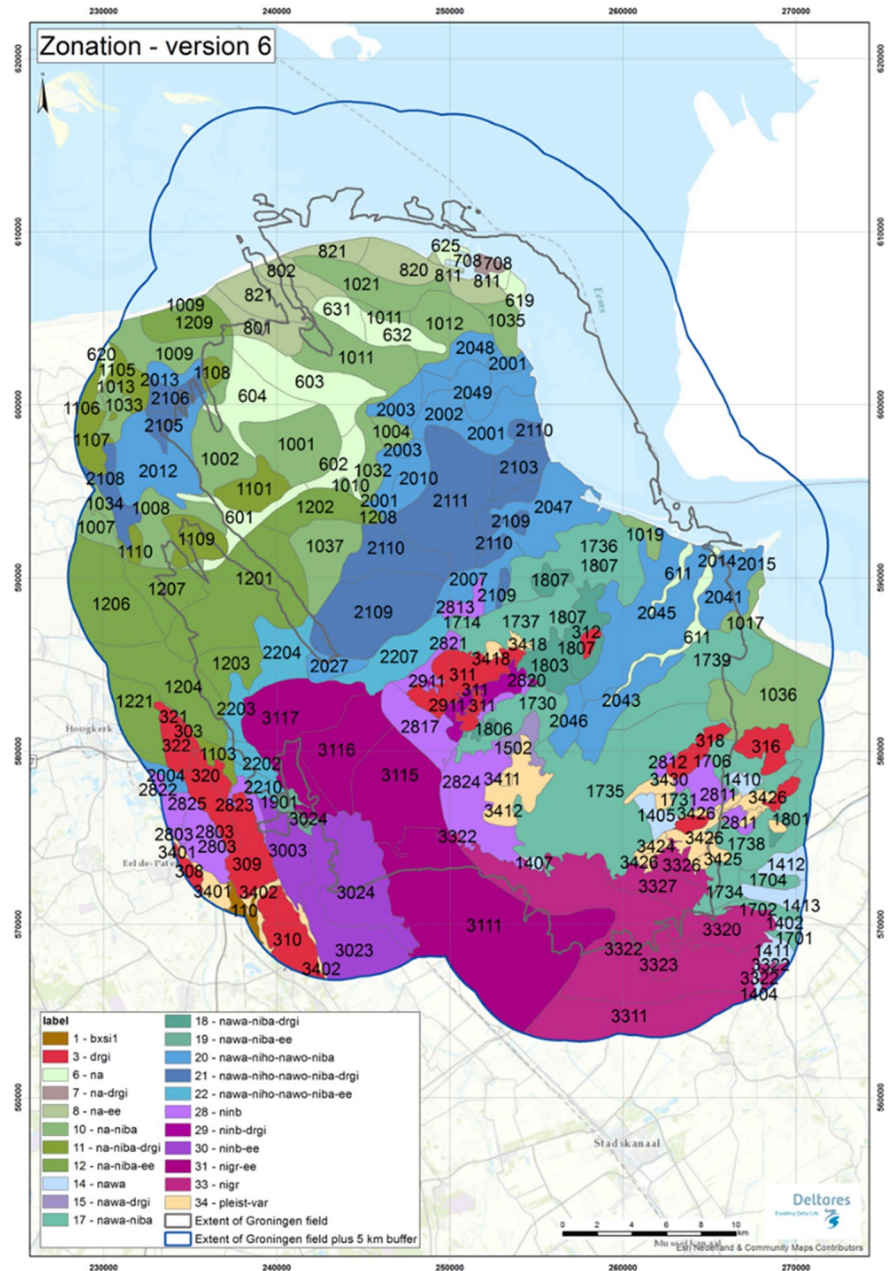
in the site response analyses, and for the modelling uncertainty. For the former, the model of Bahrampouri et al. (2019) was implemented. The modelling uncertainty was estimated from comparisons between the empirical amplification factors determined from the borehole and surface recordings at the G-stations and the calculated AFs for the same 200 m interval. The resulting terms for the modelling error are slightly lower than those found by Stewart and Afshari (2021), for example, but this may be due to the site profiles in Groningen being more amenable to 1D site response modelling than some of the Californian sites analysed in that study. The total site-to-site variability is then given by the following:

$$
\phi_{S2S} = \begin{cases} \phi_{S2S,1} & \text{for } Sa_{NS\_B} < Sa_{\text{rock,low}} \\ \phi_{S2S,1} + \left(\phi_{S2S,2} - \phi_{S2S,1}\right) \dfrac{\log\left(\frac{Sa_{NS_B}}{Sa_{\text{rock,low}}}\right)}{\log\left(\frac{Sa_{\text{rock,high}}}{Sa_{\text{rock,low}}}\right)} & \text{for } Sa_{\text{rock,low}} \leq Sa_{NS\_B} \leq Sa_{\text{rock,high}} \\ \phi_{S2S,2} & \text{for } Sa_{NS\_B} > Sa_{\text{rock,high}} \end{cases}
\tag{21}
$$

where $Sa_{\text{rock,low}}$ and $Sa_{\text{rock,high}}$ are model parameters and

$$
\begin{aligned}
\phi_{S2S,1} &= \sqrt{\left(\sigma_{lnAF,low}\right)^2 + \left(\sigma_{lnAF,MRD,lowintensity}\right)^2 + \left(\sigma_{model}\right)^2} \\
\phi_{S2S,2} &= \sqrt{\left(\sigma_{lnAF,high}\right)^2 + \left(\sigma_{lnAF,MRD,highintensity}\right)^2 + \left(\sigma_{model}\right)^2}
\end{aligned}
\tag{22}
$$

where $\sigma_{lnAF,\text{MRD}}$ is the additional uncertainty due to MRD for low and high intensity, $\sigma_{lnAF,\text{high}}$ and $\sigma_{lnAF,\text{low}}$ are the parameters of the model in Eq. (20), and σ_{model} is the model error. Since this represents both the uncertainty in the V_S profile at each voxel and the uncertainty related to the AF at any specific location relative to the zone average, both of which could be reduced by in situ measurements, the site-to-site variability in Eqs. (21) and (22) is modelled as epistemic uncertainty. This is added as a node in the logic tree (see Section 6) with three branches defined by samples of the distribution and associated weights that approximate the normal distribution (Keefer and Bodily 1983), following tests to confirm that the values conform to such a distribution.

For buildings located on dwelling mounds (locally known as wierden), an additional penalty factor is imposed on the site amplification factors (Kruiver et al. 2022a). For risk analyses using any spatially aggregated measure of damage or loss, models for the spatial

correlation of the ground motions have also been developed (Stafford et al. 2019; Kruiver et al. 2022b).

6.2 Model performance

Total residuals have been calculated for the recorded motions with respect to the V7 GMM predictions at the ground surface (Bommer et al. 2022). The fit to the data is generally very good, especially when considering that the model is developed by deconvolving motions to the NS_B using station-specific AFs but uses AFs assigned to broad zones in the forward predictions. The exception to this is the spectral acceleration at 0.01 s (which is equivalent to PGA), where the model significantly underpredicts the observed motions a consequence of calibrating the model to match the average spectral acceleration. At longer periods (0.7 s and greater), the model tends to slightly overpredict the recorded motions. These trends are of some concern, especially if the model is used to generate hazard maps of PGA, but the specific purpose of the GMM is for application in the calculation of seismic risk in the Groningen field. The parameter used to define the fragility functions is the average (geometric mean) spectral acceleration over the period range from 0.01 to 1.0 s. Figure 17 shows the residuals of the average spectral acceleration relative to the V7 GMM, from which it can be appreciated that the model performance is very good indeed.

At the same time, it is important to emphasise that the primary purpose of the GMM is not to reproduce the observed ground motions but rather to provide reliable predictions of spectral accelerations over the range of earthquake magnitude that control seismic risk in the Groningen field. The range of earthquake magnitudes contributing to the risk estimates is effectively mutually exclusive with the range of magnitudes contributing to the database. The most important feature of the model, therefore, is not that
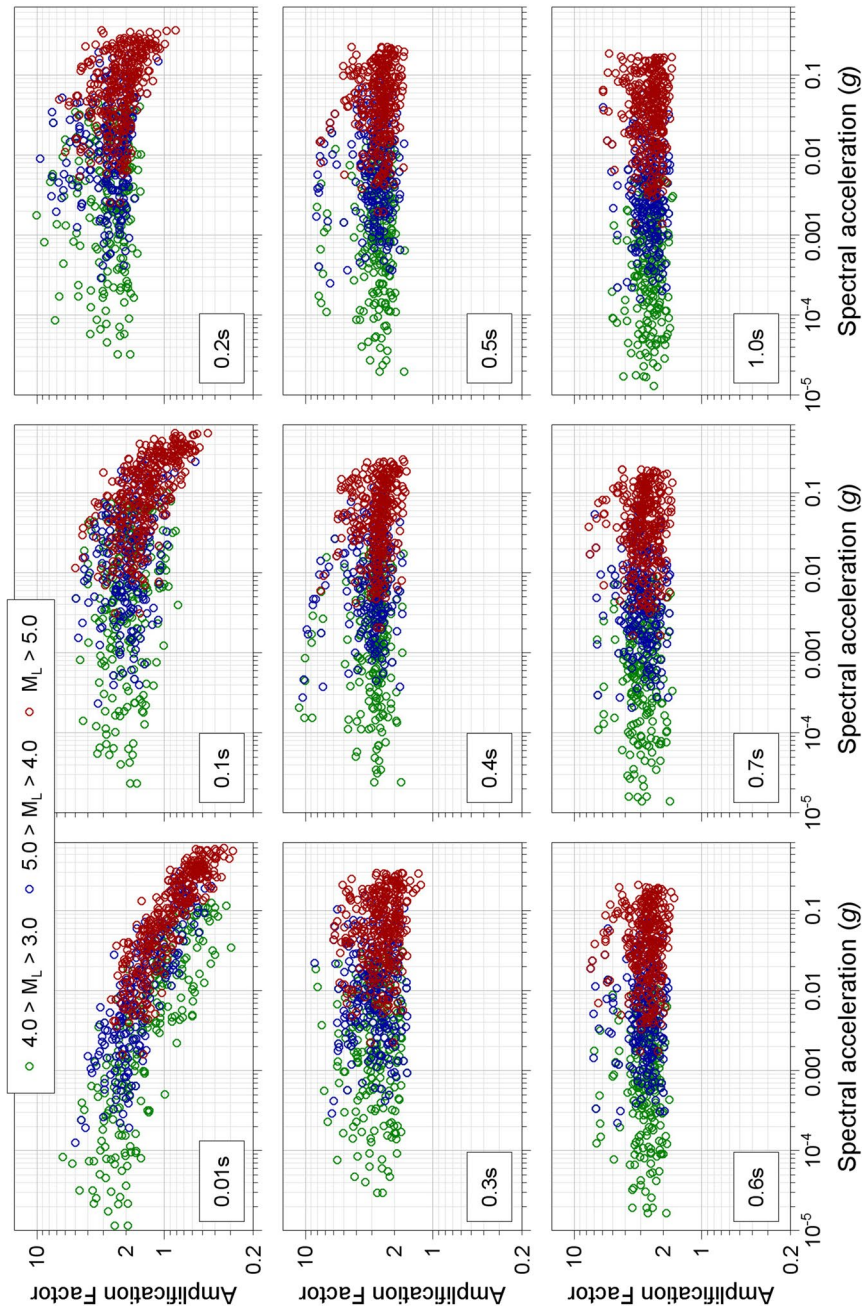
Fig. 15 Calculated AFs from site response analyses performed for the voxels within site response zone 1801, grouped by the magnitude of the scenario used to generate the input motions
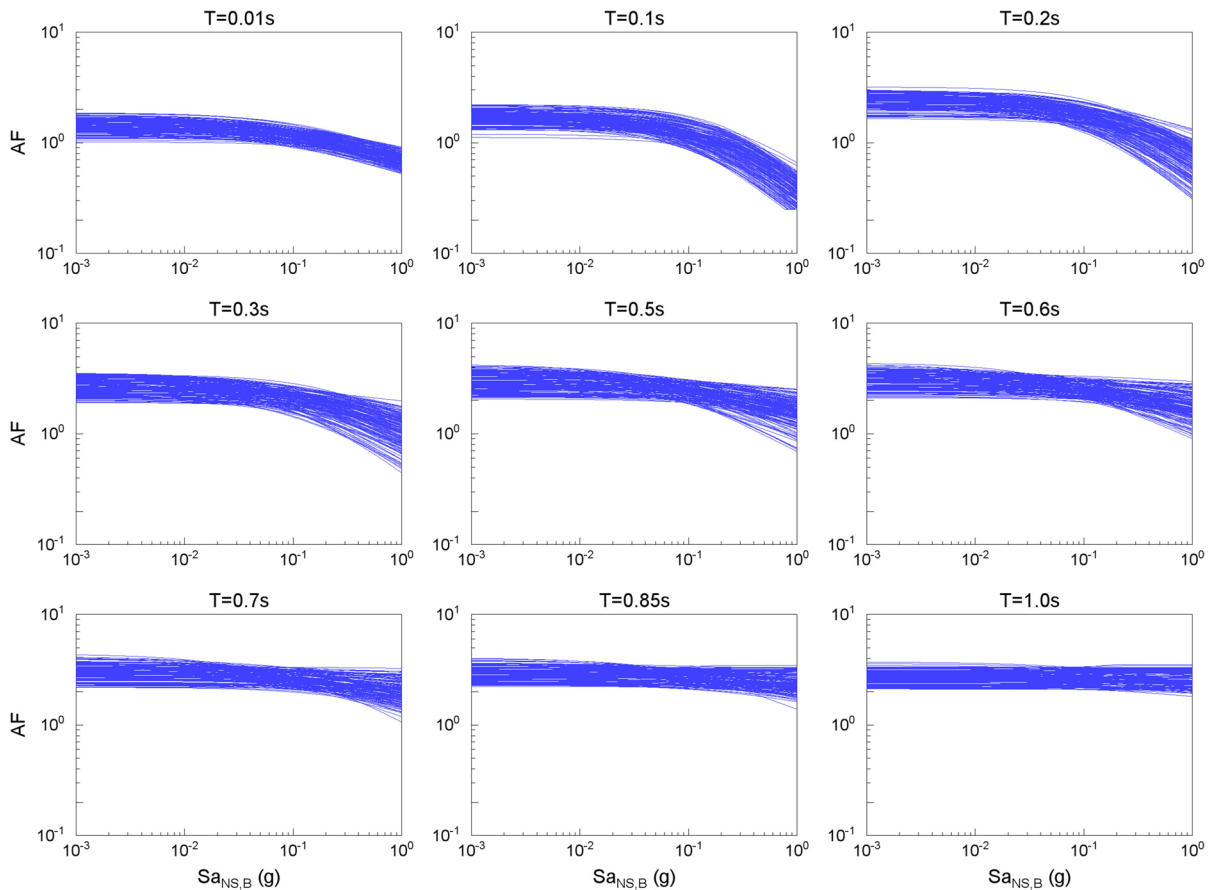
Fig. 16 AFs for all of the zones are shown in Fig. 14

it provides a perfect fit to the data—although such an outcome may be desirable—but rather that it estimates ground motions from potential larger earthquakes that reflect the source, path, and site characteristics of the field, while also capturing the epistemic uncertainty in these estimates.

7 Discussion and conclusions

Through an iterative process conducted over several years, with multiple iterations and rigorous review, ground-motion models have been developed for application to induced earthquakes in the Groningen gas field. These models include simple equations to predict PGV in the magnitude range of the events that have occurred in the field (up to M_L 3.6) and a more elaborate GMPM for application to risk analyses that consider both larger induced events and even larger

triggered earthquakes. To accommodate the epistemic uncertainty that is inevitably associated with the large extrapolations over more than three-and-half units of magnitude, the GMPM is formulated in a logic-tree framework. The complete logic tree for the model implementation is shown in Fig. 18.

The ground-motion models are very well calibrated to the characteristics of the Groningen field by virtue of extensive and intensive data collection activities that have generated a large ground-motion database and detailed characterisation of the V_S profile above the gas reservoir, with a particular focus on the near-surface layers of soft soils. While the general approaches that have been used could be adopted or adapted to other cases of induced seismicity, without such concerted efforts to gather similar datasets, there would inevitably be much larger epistemic uncertainty that would need to be accounted for in any ground-motion models.

Fig. 17 Total residuals of average spectral acceleration (between 0.01 and 1.0 s) with respect to predictions of ground motions at the surface plotted against distance
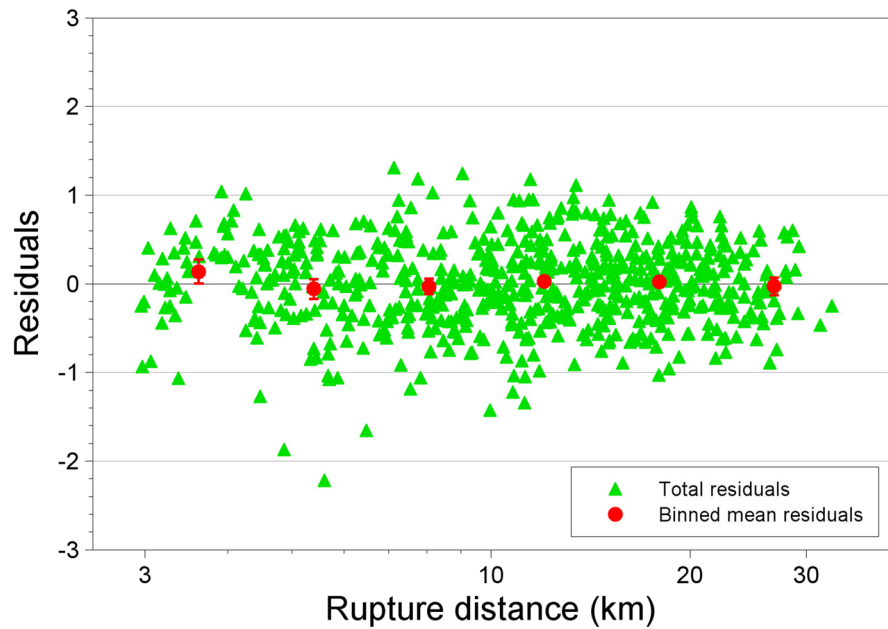
We believe that the models can be used with confidence for their intended purposes although their performance should be checked against new recordings generated by any future earthquakes in the field. There is probably little that can be done to improve the empirical GMPEs for PGV (which is based on an excellent distribution of data in the magnitude-distance to which it is applicable), although it would clearly be helpful to investigate the exact cause of the systematic differences between the motions recorded by the two different accelerograph networks. There

may, however, be scope for improving or refining the GMPM for spectral accelerations. In particularly, the underestimation of PGA needs to be addressed for applications that use this parameter, and the minor overprediction at longer periods could also be usefully investigated. The alternative procedure could also be explored for the development of the model, for example basing the NS_B reference rock model entirely on Fourier amplitude spectra. To facilitate exploration of any of these issues by interested parties, the entire database, including all the V_S,

Fig. 18 Logic tree for the Groningen GMPM for response spectral ordinates
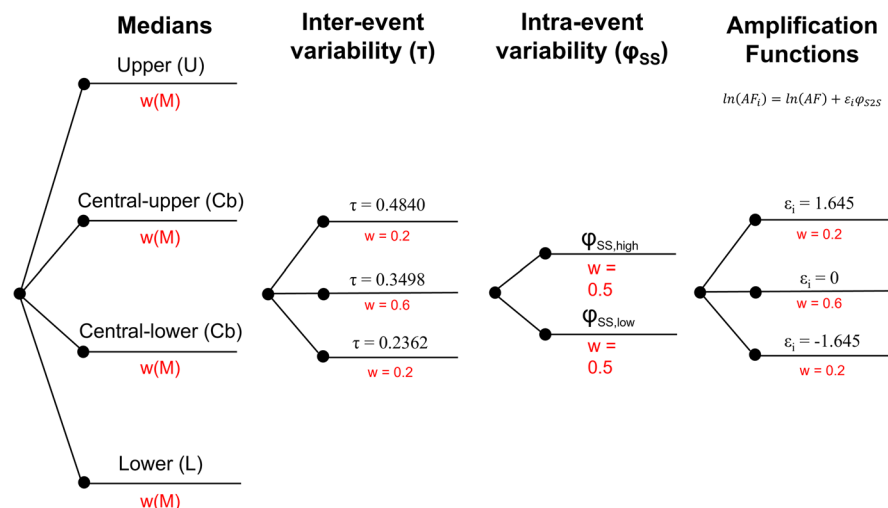
damping and lithological profiles and the associated transfer functions and amplification factors have been made freely available (Ntinalexis et al. 2022) so that others may now undertake the work of improving this model.

Some readers may question the relevance of this work in light of the political decision by the Dutch government to close the Groningen gas field (e.g. Bommer 2022). There are several reasons, however, why seismic hazard and risk assessments, and hence the ground-motion models, for the field, remain relevant. Firstly, if production ceases, it is likely that the seismicity will continue for some time until the system reaches equilibrium. Secondly, the closure of the field has been delayed because the nitrogen-mixing facility required to render imported gas similar to the low-calorific gas from the field (to which all gas-burning applications in the Netherlands are calibrated) is behind schedule. And thirdly, in view of the primary source of imported gas being Russia, recent geo-political developments may result in the decision to close the field being reversed.

Declarations

References

Abrahamson NA, Silva WJ, Kamai R (2014) Summary of the ASK14 ground motion relation for active crustal regions. Earthq Spectra 30(3):1025–1055

Akkar S, Sandıkkaya MA, Bommer JJ (2014) Empirical ground-motion models for point-and extended-source crustal earthquake scenarios in Europe and the Middle East. Bull Earthq Eng 12(1):359–387

Al Atik L (2015) NGA-East: ground-motion standard deviation models for central and eastern North America. PEER Report No. 2015/07. Pacific Earthquake Engineering Research Center, University of California at Berkeley, 217 pp

Al Atik L, Abrahamson N, Bommer JJ, Scherbaum F, Cotton F, Kuehn N (2010) The variability of ground-motion prediction models and its components. Seismol Res Lett 81(5):794–801

Anderson JG, Hough SE (1984) A model for the shape of the Fourier amplitude spectrum of acceleration at high frequencies. Bull Seismol Soc Am 74(5):1969–1993

Atkinson GM (2006) Single-station sigma. Bull Seismol Soc Am 96(2):446–455

Baker JW, Cornell CA (2006) Which spectral acceleration are you using? Earthq Spectra 22(2):293–312

Baker JW, Jayaram N (2008) Correlation of spectral acceleration values from NGA ground motion models. Earthq Spectra 24(1):299–317

Bahrampouri M, Rodriguez-Marek A, Bommer JJ (2019) Mapping the uncertainty in modulus reduction and damping curves onto the uncertainty of site amplification functions. Soil Dyn Earthq Eng 126:105091

Bindi D, Massa M, Luzi L, Ameri G, Pacor F, Puglia R, Augliera P (2014) Pan-European ground-motion prediction equations for the average horizontal component of PGA, PGV, and 5%-damped PSA at spectral periods up to 3.0 s using the RESORCE dataset. Bull Earthq Eng 12(1):391–430

Bommer JJ (2022) Earthquake hazard and risk analysis for natural and induced seismicity: towards objective assessments in the face of uncertainty. Bull Earthq Eng 20(6):2825–3069. https://doi.org/10.1007/s10518-022-01357-4

Bommer JJ, Van Elk J (2017) Comment on "The maximum possible and maximum expected earthquake magnitude for production-induced earthquakes at the gas field in Groningen, the Netherlands" by Gert Zöller and Matthias Holschneider. Bull Seismol Soc Am 107(3):1564–1567

Bommer JJ, Dost B, Edwards B, Stafford PJ, van Elk J, Doornhof D, Ntinalexis M (2016) Developing an application-specific ground-motion model for induced seismicity. Bull Seismol Soc Am 106(1):158–173

Bommer JJ, Dost B, Edwards B, Kruiver PP, Ntinalexis M, Rodriguez-Marek A, Stafford PJ, Van Elk J (2017a) Developing a model for the prediction of ground motions due to earthquakes in the Groningen gas field. Neth J Geosci 96(5):s203–s213

Bommer JJ, Stafford PJ, Edwards B, Dost B, van Dedem E, Rodriguez-Marek A, Kruiver P, van Elk J, Doornhof D, Ntinalexis M (2017b) Framework for a ground-motion model for induced seismic hazard and risk analysis in the Groningen gas field, the Netherlands. Earthq Spectra 33(2):481–498

Bommer JJ, Stafford PJ, Ntinalexis M (2021) Empirical equations for the prediction of peak ground velocity due to induced earthquakes in the Groningen gas field. 10 October 2021, https://nam-onderzoeksrapporten.data-app.nl/reports/download/groningen/en/b1512446-d4f1-48e7-ad78-dd7f950d1c6b

Bommer JJ, Edwards B, Kruiver PP, Rodriguez-Marek A, Stafford PJ, Ntinalexis M, Ruigrok E, Dost B (2022) V7 ground-motion model for induced seismicity in the Groningen gas field, Revision 1, 20 February 2022, 282 pp, available for download at https://nam-onderzoeksrappo rten.data-app.nl/reports/download/groningen/en/06766 b7a-1999-4f48-977c-33a5d94cdd82

Boore DM (2005) SMSIM–Fortran programs for simulating ground motions from earthquakes: version 2.3—a revision of OFR 96–80. US Geological Survey Open-File Report 00–509, 55 pp

Boore DM (2009) Comparing stochastic point-source and finite-source ground-motion simulations: SMSIM and EXSIM. Bull Seismol Soc Am 99(6):3202–3216

Boore DM (2010) Orientation-independent, nongeometric-mean measures of seismic intensity from two horizontal components of motion. Bull Seismol Soc Am 100(4):1830–1835

Boore DM, Stewart JP, Seyhan E, Atkinson GM (2014) NGA-West2 equations for predicting PGA, PGV, and 5% damped PSA for shallow crustal earthquakes. Earthq Spectra 30(3):1057–1085

Bourne SJ, Oates SJ, van Elk J, Doornhof D (2014) A seismological model for earthquakes induced by fluid extraction from a subsurface reservoir. J Geophys Res: Solid Earth 119(12):8991–9015

Bourne SJ, Oates SJ, Bommer JJ, Dost B, van Elk J, Doornhof D (2015) A Monte Carlo method for probabilistic hazard assessment of induced seismicity due to conventional natural gas production. Bull Seismol Soc Am 105(3):1721–1738

Bourne SJ, Oates SJ, Van Elk J (2018) The exponential rise of induced seismicity with increasing stress levels in the Groningen gas field and its implications for controlling seismic risk. Geophys J Int 213(3):1693–1700

Buijze L, Van Den Bogert PA, Wassing BB, Orlic B, Ten Veen J (2017) Fault reactivation mechanisms and dynamic rupture modelling of depletion-induced seismic events in a Rotliegend gas reservoir. Neth J Geosci 96(5):s131–s148

Camelbeeck T, Van Eck T, Pelzing R, Ahorner L, Loohuis J, Haak HW, Hoang-Trong P, Hollnack D (1994) The 1992 Roermond earthquake, the Netherlands, and its aftershocks. Geol Mijnbouw 73:181–197

Campbell KW, Bozorgnia Y (2007) Campbell-Bozorgnia NGA ground motion relations for the geometric mean horizontal component of peak and spectral ground motion parameters. PEER Report 2007/02, Pacific Earthquake Engineering Research Center, University of California at Berkeley, 240 pp

Campbell KW, Bozorgnia Y (2014) NGA-West2 ground motion model for the average horizontal components of PGA, PGV, and 5% damped linear acceleration response spectra. Earthq Spectra 30(3):1087–1115

Cavalieri F, Correia AA, Pinho R (2021) Variations between foundation-level recordings and free-field earthquake ground motions: numerical study at soft-soil sites. Soil Dyn Earthq Eng 141:106511

Chiou BS, Youngs RR (2014) Update of the Chiou and Youngs NGA model for the average horizontal component of peak ground motion and response spectra. Earthq Spectra 30(3):1117–1153

Crowley H, Pinho R, Polidoro B, van Elk J (2017a) Developing fragility and consequence models for buildings in the Groningen field. Neth J Geosci 96(5):s247–s257

Crowley H, Polidoro B, Pinho R, van Elk J (2017b) Framework for developing fragility and consequence models for local personal risk. Earthq Spectra 33(4):1325–1345

Crowley H, Pinho R, van Elk J, Uilenreef J (2019) Probabilistic damage assessment of buildings due to induced seismicity. Bull Earthq Eng 17(8):4495–4516

Darendeli M (2001) Development of a new family of normalized modulus reduction and material damping curves. Ph.D. Thesis, Dept. of Civil Eng., University of Texas, Austin, TX

Dost B, Van Eck T, Haak H (2004) Scaling of peak ground acceleration and peak ground velocity recorded in the Netherlands. Bollettino Di Geofisica Teorica Ed Applicata 45(3):153–168

Dost B, Ruigrok E, Spetzler J (2017) Development of seismicity and probabilistic hazard assessment for the Groningen gas field. Neth J Geosci 96(5):s235–s245

Dost B, Edwards B, Bommer JJ (2018) The relationship between $\mathbf{M}$ and M_L: a review and application to induced seismicity in the Groningen Gas Field, The Netherlands. Seismol Res Lett 89(3):1062–1074

Dost B, Edwards B, Bommer JJ (2019) Erratum: The relationship between $\mathbf{M}$ and M_L: a review and application to induced seismicity in the Groningen Gas Field, The Netherlands. Seismol Res Lett 90(4):1660–1662

Dufumier H, Michelini A, Du Z, Bondar I, Sileny J, Mao W, Kravanja S, Panza GF (1997) Regional structure modelling and source inversion for the 1992 Roermond earthquake. J Seismolog 1(4):321–340

Edwards B, Ntinalexis M (2021) Defining the usable bandwidth of weak-motion records: application to induced seismicity in the Groningen Gas Field, the Netherlands. J Seismolog 25(4):1043–1059

Edwards B, Zurek B, Van Dedem E, Stafford PJ, Oates S, Van Elk J, DeMartin B, Bommer JJ (2019) Simulations for the development of a ground motion model for induced seismicity in the Groningen gas field, The Netherlands. Bull Earthquake Eng 17(8):4441–4456

Haak HW, Meidow H, Ahorner L, Verbeiren R, Hoang-Trong P, Musson RM, Henni P, Schenkova Z, Zimova R (1994) The macroseismic map of the Roermond earthquake of April 13, 1992. Geologij En Mijnbouw 73:265–270

Hollender F, Roumelioti Z, Maufroy E, Traversa P, Mariscal A (2020) Can we trust high-frequency content in strong-motion database signals? Impact of housing, coupling, and installation depth of seismic sensors. Seismol Res Lett 91(4):2192–2205

Keefer DL, Bodily SE (1983) Three-point approximations for continuous random variables. Manage Sci 29(5):595–609

Kottke AR, Rathje EM (2008) Technical Manual for Strata. PEER Report 2008/10, Pacific Earthquake Engineering Research Center, University of California at Berkeley, February, 84 pp

Kraaijpoel D, Dost B (2013) Implications of salt-related propagation and mode conversion effects on the analysis of induced seismicity. J Seismol 17(1):95–107

Kruiver PP, van Dedem E, Romijn R, de Lange G, Korff M, Stafleu J, Gunnink JL, Rodriguez-Marek A, Bommer JJ, van Elk J, Doornhof D (2017a) An integrated shear-wave velocity model for the Groningen gas field, The Netherlands. Bull Earthquake Eng 15(9):3555–3580

Kruiver PP, Wiersma A, Kloosterman FH, de Lange G, Korff M, Stafleu J, Busschers FS, Harting R, Gunnink JL, Green RA, van Elk J (2017b) Characterisation of the Groningen subsurface for seismic hazard and risk modelling. Neth J Geosci 96(5):s215–s233

Kruiver PP, Pefkos M, Meijles E, Aalbersberg G, Chapman X, van der Ween W, Martin A, Ooms-Asshoff K, Bommer JJ, Rodriguez-Marek A, Pinho R (2022a) Incorporating dwelling mounds into induced seismic risk analysis for the Groningen gas field in the Netherlands. Bull Earthq Eng 20(1):255–285

Kruiver PP, Pefkos M, Rodriguez-Marek A, Chapman X, Ooms-Asshoff K, Chmiel M, Lavoué A, Stafford PJ, van Elk J (2022b) Capturing spatial variability in the regional ground motion model for Groningen. Netherlands Journal of Geoscience 101(e16) https://doi.org/10.1017/njg.2022.13

Motazedian D, Atkinson GM (2005) Stochastic finite-fault modeling based on a dynamic corner frequency. Bull Seismol Soc Am 95(3):995–1010

Menq FY (2003) Dynamic properties of sandy and gravelly soils, PhD Thesis, Department of Civil Engineering, University of Texas, Austin, TX

NIST (2012). Soil-structure interaction for building structures. Report NIST GCR 12–917–21, National Institute of Standards and Technology, US Department of Commerce, 292 pp

Noorlandt R, Kruiver PP, de Kleine MP, Karaoulis M, de Lange G, Di Matteo A, von Ketelhodt J, Ruigrok E, Edwards B, Rodriguez-Marek A, Bommer JJ (2018) Characterisation of ground motion recording stations in the Groningen gas field. J Seismolog 22(3):605–623

Ntinalexis M, Bommer JJ, Ruigrok E, Edwards B, Pinho R, Dost B, Correia AA, Uilenreef J, Stafford PJ, van Elk J (2019) Ground-motion networks in the Groningen field: usability and consistency of surface recordings. J Seismolog 23(6):1233–1253

Ntinalexis M, Kruiver PP, Bommer JJ, Ruigrok E, Rodriguez-Marek A, Edwards B, Pinho R, Spetzler J, Obando Hernandez E, Pefkos M, Bahrampouri M, van Onselen EP, Dost B, van Elk J (2022) A database of ground-motion recordings, site profiles, and amplification factors from the Groningen gas field in the Netherlands. Submitted to Earthquake Spectra

Parker GA, Stewart JP (2021) Ergodic site response model for subduction zone regions. Earthq Spectra. https://doi.org/10.1177/87552930211056963

Parker GA, Stewart JP, Hashash YM, Rathje EM, Campbell KW, Silva WJ (2019) Empirical linear seismic site amplification in central and eastern North America. Earthq Spectra 35(2):849–881

Rathje EM, Ozbey MC (2006) Site-specific validation of random vibration theory-based seismic site response analysis. J Geotech Geoenviron Eng 132(7):911–922

Rodriguez-Marek A, Cotton F, Abrahamson NA, Akkar S, Al Atik L, Edwards B, Montalva GA, Dawood HM (2013) A model for single-station standard deviation using data from various tectonic regions. Bull Seismol Soc Am 103(6):3149–3163

Rodriguez-Marek A, Kruiver PP, Meijers P, Bommer JJ, Dost B, van Elk J, Doornhof D (2017) A regional site-response

model for the Groningen gas field. Bull Seismol Soc Am 107(5):2067–2077

Ruigrok E, Rodriguez-Marek A, Edwards B, Kruiver PP, Dost B, Bommer JJ (2022) Derivation of a near-surface damping model for the Groningen gas field. Geophys J Int. https://doi.org/10.1093/gji/ggac069

Spetzler J, Dost B (2017) Hypocentre estimation of induced earthquakes in Groningen. Geophys J Int 209(1):453–465

Stafford PJ, Rodriguez-Marek A, Edwards B, Kruiver PP, Bommer JJ (2017) Scenario dependence of linear site-effect factors for short-period response spectral ordinates. Bull Seismol Soc Am 107(6):2859–2872

Stafford PJ, Zurek BD, Ntinalexis M, Bommer JJ (2019) Extensions to the Groningen ground-motion model for seismic risk calculations: component-to-component variability and spatial correlation. Bull Earthq Eng 17(8):4417–4439

Stewart JP, Afshari K (2021) Epistemic uncertainty in site response as derived from one-dimensional ground response analyses. J Geotech Geoenviron Eng 147(1):04020146

Stewart JP, Afshari K, Hashash YMA (2014) Guidelines for performing hazard-consistent one-dimensional ground response analysis for ground motion prediction. PEER Report 2014/16, Pacific Earthquake Engineering Research Center, University of California, Berkeley, CA

van Eck T, Goutbeek F, Haak H, Dost B (2006) Seismic hazard due to small-magnitude, shallow-source, induced earthquakes in The Netherlands. Eng Geol 87(1–2):105–121

van Eijs RM, Mulders FM, Nepveu M, Kenter CJ, Scheffers BC (2006) Correlation between hydrocarbon reservoir properties and induced seismicity in the Netherlands. Eng Geol 84(3–4):99–111

van Elk J, Doornhof D, Bommer JJ, Bourne SJ, Oates SJ, Pinho R, Crowley H (2017) Hazard and risk assessments for induced seismicity in Groningen. Neth J Geosci 96(5):s259–s269

van Elk J, Bourne SJ, Oates SJ, Bommer JJ, Pinho R, Crowley H (2019) A probabilistic model to evaluate options for mitigating induced seismic risk. Earthq Spectra 35(2):537–564

Wells DL, Coppersmith KJ (1994) New empirical relationships among magnitude, rupture length, rupture width, rupture area, and surface displacement. Bull Seismol Soc Am 84(4):974–1002

Zwanenburg C, Konstadinou M, Meijers P, Goudarzy M, König D, Dyvik R, Carlton B, Elk JV, Doornhof D, Korff M (2020) Assessment of the dynamic properties of holocene peat. J Geotech Geoenviron Eng 146(7):04020049